Manuscript submitted to Continental Shelf Research:

Outer shelf seafloor geomorphology along a carbonate escarpment: The eastern Malta Plateau, Mediterranean Sea.

Aaron Micallef[a]*, Aggeliki Georgiopoulou[b,c], Joshu Mountjoy[d], Veerle A.I. Huvenne[e], Claudio Lo Iacono[e], Timothy Le Bas[e], Paola Del Carlo[f], Daniel Cunarro Otero[a]

[a] Marine Geology and Seafloor Surveying, Department of Geosciences, University of Malta, Msida, MSD 2080, Malta.

[b] UCD School of Earth Sciences, University College Dublin, Dublin, Ireland.

[c] UCD Earth Institute, University College Dublin, Dublin, Ireland.

[d] National Institute of Water and Atmospheric Research, Wellington, New Zealand.

[e] Marine Geoscience, National Oceanography Centre, University of Southampton Waterfront Campus, European Way, Southampton, UK.

[f] Istituto Nazionale di Geofisica e Vulcanologia, Sezione di Pisa, via della Faggiola 32, 56126, Pisa Italy.

*Corresponding author:

E-mail: aaron.micallef@um.edu.mt; Telephone: +356 23403613.

ABSTRACT

Submarine carbonate escarpments, documented in numerous sites around the world, consist of thick exposures of Mesozoic shallow water carbonate sequences - primarily limestones and dolomites - with reliefs of >1 km and slope gradients of >70°. Whilst most research efforts have focused on the processes that shaped carbonate escarpments into complex and extreme terrains, little attention has been paid to the geomorphology of shelves upslope of carbonate escarpments. In this study we investigate high resolution geophysical, sedimentological and visual data acquired from the eastern Malta Plateau, central Mediterranean Sea, to demonstrate that the outer shelf of a carbonate escarpment is directly influenced by escarpment-forming processes. We document forty eight erosional scars, six long channels and numerous smaller-scale channels, three elongate mounds, and an elongate ridge across the eastern Malta Plateau. By analysing their morphology, seismic character, and sedimentological properties, we infer that the seafloor of the eastern Malta Plateau has been modified by three key processes: (i) Mass movements – in the form of translational slides, spreading and debris flows – that mobilised stratified Plio-Pleistocene hemipelagic mud along the shelf break and that were likely triggered by seismicity and loss of support due to canyon erosion across the upper Malta Escarpment; (ii) NNW-SSE trending sinistral strike-slip deformation in Cenozoic carbonates – resulting from the development of a mega-hinge fault system along the Malta Escarpment since the Late Mesozoic, and SE-NW directed horizontal shortening since the Late Miocene – which gave rise to NW-SE oriented extensional grabens and a NNW-SSE horst; (iii) Flow of bottom currents perpendicular and parallel to the Malta Escarpment, associated with either Modified Atlantic Water flows

during sea level lowstands and/or Levantine Intermediate Water flows at present, which was responsible for sediment erosion and deposition in the form of channels and contouritic drifts.

Keywords: submarine landslide; fault; contouritic drift; carbonate escarpment; outer shelf; Malta Plateau

1. INTRODUCTION

Submarine carbonate escarpments - limestone and dolomite cliffs with relief in excess of 1 km and slope gradients exceeding 70° – have been documented at numerous sites around the world (e.g. Apulia (Volpi et al., 2011), Bahamas (Freeman-Lynde et al., 1981), Blake (Paull and Dillon, 1980), Campeche (Paull et al., 2014), Florida (Paull et al., 1990; Twichell et al., 1990), Grand Banks (Ryan and Miller, 1981), Malta (Micallef et al., in review; Scandone et al., 1981) Escarpments). Such escarpments expose thick stratigraphic sequences of Mesozoic shallow water carbonate accumulations. These outcrops have been eroded into complex and extreme terrains - comprising wide canyons, landslide scars, vertical walls and overhangs – by a variety of processes (e.g. gravity flows, fluid seepage, submarine landslides, bottom currents and biological activity (Paull and Dillon, 1980; Paull and Neumann, 1987; Twichell et al., 1996)).

Such conspicuous landforms have a strong influence on the surrounding seafloor, particularly abyssal plains. Downslope erosion by gravity flows results in the formation of plunge pools and turbidite deposits at the base of escarpments (Micallef et al., in review). Slope failures generate extensive mass movement deposits (Brooks et al., 1986; Halley and Schlager, 1983; Mullins et

al., 1986; Paull et al., 2014; Twichell et al., 1990), whereas escarpment retreat results in erosional benches at the base (Paull and Dillon, 1980). Topographic focusing of ocean currents along the escarpment can form erosional moats (Dillon et al., 1987; Land et al., 1999; Paull and Dillon, 1980), contouritic drifts (Micallef et al., in review), and sediment waves (Gutscher et al., 2016). Fluid seepage at the base of the escarpment can generate fan-shaped sediment deposits that include pyrite and sulphide (Commeau et al., 1987; Paull et al., 1992; Paull et al., 1990).

Very little attention has been paid to the impact of carbonate escarpments on adjacent continental shelves. In this study we show that the outer shelf of a carbonate escarpment can host a wide range of morphologies that are predominantly influenced by escarpment-forming processes. We demonstrate this by analysing high resolution geophysical, sedimentological and visual data acquired from the eastern Malta Plateau, central Mediterranean Sea, between 2012 and 2014. Using these data we: (i) document the key landforms across the eastern Malta Plateau, and (ii) determine the nature and origin of the processes responsible for their formation.

2. REGIONAL SETTING

The Pelagian Platform is a structural unit of the African foreland colliding with the European plate. It forms a shallow shelf between south Sicily and north-west Libya that separates the deep Ionian Basin from the Western Mediterranean. The Malta Plateau is a 150 km long and 120 km wide ridge located in the north-eastern part of the Pelagian Platform (Figure 1). It is characterised by a smooth and gently sloping seafloor that is predominantly 100-150 m in depth, although it locally reaches depths of 400 m. The continental basement of the Malta Plateau is overlain by a

90 >4500 m thick sequence of limestones, dolomites and volcanic deposits, ranging from Upper
91 Triassic to late Neogene in age (Jongsma et al., 1985; Torelli et al., 1995). More recent sediments
92 covering the Neogene succession comprise parallel-bedded units of Plio-Pleistocene terrestrial,
93 pelagic and hemipelagic sediments that are up to 300 m thick (Max et al., 1993; Osler and Algan,
94 1999). The basement of these units is the Messinian low-stand erosional surface.
95
96 During the Early to Middle Jurassic phase, the Pelagian Platform underwent a major extensional
97 phase, as demonstrated by the widespread occurrence of volcanic rocks dating to this epoch
98 (Scandone et al., 1981). During the Middle to Upper Cretaceous, the Pelagian Platform was
99 dominated by quiet tectonic conditions marked by gentle subsidence along former rift zones
100 (Finetti, 1982; Gardiner et al., 1995). In view of the change in the direction of movement the
101 African Plate with respect to the Eurasian Plate, the Upper Cretaceous was characterised by
102 renewed extension, subsidence and widespread volcanic activity. During the Tertiary, the tectonic
103 regime changed to a compressive one due to the collision between the African and the Eurasian
104 plates along the Maghrebian thrust front (Lipparini et al., 2009). In spite of this tectonic regime,
105 the period between the Miocene and Quaternary is characterised by an extensional phase (Finetti,
106 1982; Gardiner et al., 1995). On the western part of the Malta Plateau, this period is associated
107 with the development of the Sicily Channel Rift Zone, which entails a system of three NW–SE
108 trending grabens (Pantelleria, Malta and Linosa Grabens) where water depth reaches a maximum
109 of around 1700 m (Reuther and Eisbacher, 1985). These grabens are governed by a fault system
110 that extends throughout the Sicily Channel, from Southern Sicily to Tunisia (Illies, 1981). Rifting
111 was accompanied by extensive igneous activity, which resulted in the volcanic islands of
112 Pantelleria and Linosa.

To the east, the Malta Plateau is separated from the Ionian Basin by the Malta Escarpment, a 290 km long and 3.2 km high cliff that extends southwards from eastern Sicily and that reaches local slope gradients of 74° (Figure 1). The escarpment is an inherited structural feature from the early Mesozoic (Casero et al., 1984; Cita et al., 1980; Finetti, 1982; Grasso, 1993; Nicolich et al., 2000; Reuther et al., 1993; Scandone et al., 1981). It is thought to have originated by rifting in the Upper Permian-Triassic, which was followed by spreading from the Jurassic till the Upper Cretaceous-early Palaeogene (Catalano et al., 2000a; Grasso, 1993). The escarpment exhibits both Mesozoic normal block faulting and a more recent sinistral strike-slip component. The latter is likely related to the conversion of the Malta Escarpment from a passive margin to a mega-hinge fault system in the Late Mesozoic, and from SE-NW directed horizontal shortening since the Late Miocene (Adam et al., 2000; Reuther, 1990; Reuther et al., 1993; Reuther and Eisbacher, 1985). These changes in the tectonic stress field of the area are attributed to plate convergence between Africa and Europe, and differences in convergence rates of the Pelagian continental crust and the adjacent Ionian oceanic crust (Adam et al., 2000; Argnani and Bonazzi, 2005; Catalano and Sulli, 2006; Gutscher et al., 2016). More recent structural deformation has been restricted to the segment of the escarpment north of Siracusa (Argnani and Bonazzi, 2005). The Malta Escarpment is also characterised by erosional scars and a dense network of narrow and wide canyons. These are attributed to dissolution by fluid seepage, terrestrial fluvial erosion during the Messinian Salinity Crisis, gravity flow erosion, and multi-scale slope failures (Micallef et al., in review).

135 The Malta Plateau is also bound by the Hyblean Plateau of mainland Sicily to the north and a
136 Plio-Quaternary foredeep of the Maghrebian fold-and-thrust belt to the west (Gela Basin). Direct
137 evidence of fluid flow and seepage systems have been reported in several parts of the Malta
138 Plateau (Holland et al., 2003; Max et al., 1993; Micallef et al., 2011; Savini et al., 2009).
139
140 The Pelagian Platform represents a main pathway for Atlantic waters that enter through the
141 Gibraltar Strait (Modified Atlantic Water, MAW) (Millot and Taupier-Letage, 2005) (Figure 1).
142 The upper 100-120 m of the water column in the Pelagian Platform consists of the MAW flowing
143 towards the east. Across the Malta Plateau, the MAW flows in a south-easterly direction at
144 velocities of up to 25 cm s^{-1} (Lermusiaux and Robinson, 2001). The more saline Levantine
145 Intermediate Water (LIW), which originates in the eastern basin, splits into two flows -
146 westwards below the MAW, and northwards along the eastern flank of the Malta Plateau. In the
147 latter case, the LIW flow reaches velocities of up to 20 cm s^{-1} (Lermusiaux and Robinson, 2001).
148
149 FIGURE 1
150
151 **3. MATERIALS AND METHODS**
152
153 We base our study on six types of seafloor data acquired during the CUMECS (2012) and
154 CUMECS-2 (2014) research cruises. These include:
155
156 (i) Multibeam echosounder (MBES) data: An area of ~950 km^2 of seabed within a depth
157 range of 100 – 1200 m was surveyed using a Kongsberg-Simrad EM-710 system and

158 Reson SeaBat 7150 and 8111 systems. Grids with 10 m × 10 m bin size were derived for
159 both bathymetry and backscatter (Figure 2). Bathymetry data were processed by
160 accounting for sound velocity variations and basic quality control using CARIS HIPS and
161 SIPS. The backscatter data were processed with PRISM (Processing of Remotely-sensed
162 Imagery for Seafloor Mapping) software (Le Bas and Hühnerbach, 1998). Processing
163 included radiometric corrections, geometric corrections and mosaicking. Standard
164 morphometric attributes and morphometric maps (Micallef et al., 2007a) were generated
165 to map landforms across the study area.

166 (ii) Sub-bottom profiles: High resolution sub-bottom profiles were acquired simultaneously
167 with the MBES data. The profiles were collected using a hull-mounted Datasonics
168 CHIRP-II profiler operating at frequencies of 2-7 kHz.

169 (iii) Single-channel seismic reflection profiles: 120 km of Sparker profiles were acquired
170 from the central part of the study area using a 1 kJ multi-component Geo-Resources
171 Geospark 1500 system triggered at 1 s intervals (Figure 3). Seismic data processing was
172 carried out with Seismic Processing Workshop and Hotshot, and included filtering and
173 amplitude corrections.

174 (iv) Remotely Operated Vehicle (ROV) surveys: Two dives were carried out using the
175 PolluxIII system, which has a maximum 600 m operating depth capability and a forward-
176 looking 1/3" Sony Charge Coupling Device colour video camera (Figure 3). The first
177 survey (ROV1) lasted approximately 5 h, covering a distance of 2.7 km and a depth range
178 from 300 to 537 m. The second survey (ROV2) lasted approximately 2 h, covering a
179 distance of 1.4 km and a depth range from 285 to 496 m.

(v) Dredge samples: Dredge samples were acquired with a cylindrical metallic dredge along the ROV1 transect at a depth of 320 m.

(vi) Gravity cores: A total of 28 m of sediment cores were obtained from nine sites (Figure 3) using a 6-m gravity corer configured with a trigger weight and pelican set-up. Analyses of the sediment cores included the following:

- The cores were visually logged, photographed, and analysed in terms of sediment colour, magnetic susceptibility, P-wave velocity, and gamma density using a Geotek® Multi-Sensor Core Logger at the National Oceanography Centre, Southampton.
- Samples from selected intervals in the cores were analysed quantitatively for grain size distributions with a Malvern Mastersizer 2000 (Malvern Instruments Limited, Malvern, UK) in combination with a Malvern Hydro G accessory unit and 36-pot Malvern auto-sampler. The instrument uses laser diffraction to calculate grain diameters between 0.02 μm and 2000 μm.
- Undrained shear strength measurements (in kPa) were obtained from four cores (CU12_01, CU12_02, CU12_07, CU12_10) at 20 cm intervals using a hand held shear vane tester.
- AMS ^{14}C dating of four samples from two cores (CU12_01, CU12_07) was carried out by the Poznań Radiocarbon Laboratory. Foraminiferal mixed assemblages of both *Globigerinoides ruber* and *Globigerina bulloides* were used, as there were not enough individuals for monospecific picking to make up the necessary 5 mg of clean shell material required for these measurements.
- Volcanic ash layers represent valuable stratigraphic tools for geological correlation and dating when they are distinctive and sufficiently widespread (Lowe (2011) and

references therein). Tephra layers within the cores were sampled and analysed for textural and components analyses using a Scanning Electron Microscope (SEM) Zeiss EVO MA 10 at the Istituto Nazionale di Geofisica e Vulcanologia Sezione di Pisa, and for geochemical analyses of glass using a JEOL JXA-8600 microprobe (EMP) equipped with 4 wavelength dispersive spectrometers at IGG-CNR Firenze.

FIGURE 2

FIGURE 3

4. RESULTS

4.1 Seafloor morphology and sub-seafloor character

The seafloor across the eastern Malta Plateau is predominantly smooth, very gently sloping (0.8° - 1.8°) towards the east, and characterised by low backscatter response (Figures 2, 3). ROV imagery shows a terrain predominantly covered by a drape of fine-grained sediment with variable levels of bioturbation. The shelf break between the eastern Malta Plateau and the upper Malta Escarpment occurs at depths ranging from 100 m in the north, where it is quite angular and sharp, to 400 m in the south, where the shelf break is generally more curved and smooth.

The seismic expression of the sub-seafloor in most of the eastern Malta Plateau comprises an up to 0.2 s (Two Way Travel Time (TWTT)) thick sequence of continuous, parallel, high amplitude seismic reflectors (facies 2A) sloping towards the shelf edge (Figure 4a). The sequence becomes thinner towards the shelf edge. The sequence of parallel seismic reflectors is underlain by an acoustically transparent facies of variable thickness (facies 3) (Figure 4a). The top of this facies comprises a low amplitude seismic reflector, which is generally irregular and locally incised by depressions. At the few sites where the overburden is thin, the seafloor is characterised by a hummocky topography (Figure 4c).

Seafloor shallower than 140 m is characterised by a widespread and distinctive angular unconformity (unconformity 1, Figure 4b), where high amplitude, parallel seismic reflectors that

slope towards the Malta Escarpment (facies 2A) are truncated and covered by up to 0.01 s (TWTT) thick transparent seismic facies that lacks any internal reflectors (facies 1).

FIGURE 4

There are four distinct morphologic elements that characterise the eastern Malta Plateau seafloor (Figure 5a).

FIGURE 5

4.1.1 Erosional scars

The southern half of the study area is affected by forty eight scars that range from 0.2 to 70 km^2 in area (mean of 2.2 km^2) (Figure 5a). The scars have arcuate to elongate planform shapes (both across- and along-slope). The lateral and upslope limits of the largest scars are characterised by escarpments with gradients of up to 17°, heights of up to 80 m and high backscatter response (Figures 6, 7). The downslope limit of all the scars is contiguous with other features, such as another scar, a depression, or the edge of the Malta Plateau.

The largest scars have contrasting morphologies. Scar S1, which is located upslope of Cumecs Canyon in the southern part of the study area, has a 6.5 km wide and 25 km long crescent planform shape (Figure 6a). The seafloor within the scar is generally smooth, gently sloping (1.5°), and characterised by low backscatter (Figure 6b). The escarpment bounding the scar

displays very high backscatter (Figure 6b). Scar S2, which is also located upslope of the Cumecs Canyon in the central part of the study area, is 7.7 km long and up to 3 km wide (Figure 7a). It comprises a series of sub-parallel linear ridges (up to 1.5 km long and 12 m high) and troughs. The ridges and troughs become less widely spaced and shorter with distance downslope. In the south-eastern section, the scar leads to a channel (C5) with smooth seafloor and almost flat bottom. Scar S2 has a predominantly low backscatter response, but some of the ridge flanks correspond to moderate backscatter (Figure 7c).

The other scars are considerably smaller and comprise smooth, near-planar seafloor. Occasionally, the upslope section comprises a ridge and trough pattern that is significantly smaller and less pronounced than that in scar S2. Another twenty four scars occur on the upper Malta Escarpment, and a sediment core was obtained from one of these (CU12_02 from scar S5) (Figure 8a).

FIGURE 6

FIGURE 7

FIGURE 8

Seismic reflection profiles show that the sequence of continuous, parallel, high amplitude seismic reflections characterising the eastern Malta Plateau (facies 2A) is truncated by the scar escarpments (Figure 7b). Up to 0.1 s (TWTT) of the sub-seafloor has been affected by the scars.

The seismic signature of the downslope section of the scars is generally hummocky to chaotic (facies 2D; Figure 8b). Where ridges and troughs occur, the seismic facies is predominantly characterised by irregular, partly chaotic facies of variable thickness (facies 2C - up to 0.06 s (TWTT)) (Figure 7b). The base of the irregular, partly chaotic facies is a planar, continuous, high amplitude reflector. This base reflector is the same one for scars S2 and S3 (Figures 7b; 11); it is found between 0.02 s and 0.15 s (TWTT) below the seafloor, and its depth decreases towards the shelf without outcropping across the study area. The imaged scars are draped by an up to 0.006 s (TWTT) thick sequence of coherent, moderate amplitude reflectors.

4.1.2 Channels

The central part of the study area is incised by six channels that reach the Malta Escarpment (Figure 5a). The longest of these (C4) is 12 km long, up to 1.6 km wide and 120 m deep (Figure 9a). The channel axis is characterised by medium to very low backscatter. The cross-sectional profile of the channel is asymmetric, with the northern wall being steeper (+3°) and higher (+100 m) than the southern wall (Figure 9c). The eastern section of the northern wall is characterised by very steep terrain (>60°) and high backscatter (Figure 2b). The channel walls are affected by numerous small scars (150 – 700 m in length), all of which slope towards and connect to the axis of the channel. The scars are shallow (maximum depth of 5 m), smooth, planar and have low aspect ratios. Seismic reflection profiles intersecting channel C4 show an up to 0.18 s (TWTT) sequence of continuous, parallel, high amplitude seismic reflectors (facies 2A) that slope towards, and converge at the channel axis (Figure 9b). The sequence across the southern wall is thicker

than that on the northern wall. Underlying this sequence is an irregular, discontinuous and low amplitude reflector, below which the seismic facies is transparent (facies 3).

FIGURE 9

There are other channels in the area but they are shorter and have more subdued morphologies (Figure 5a). Channels C1 and C2 also show asymmetric profiles like C4, whereas that of C3 breaks the pattern and its southern wall is steeper than the northern wall. The westernmost edges of channels C2 and C3 are connected by a SW-NE trending escarpment that faces SE and is 50 m high. The southernmost two channels (C5 and C6) are the shortest and connect scars S2 and S4 with the upper Malta Escarpment (Figure 5a).

Numerous smaller scale channels (up to 5.5 km long and 0.2 km wide), characterised by high backscatter, incise the seafloor in scar S1 (Figure 6b).

4.1.3 Elongate mounds

The northern wall of channel C4 is bound by a W-E oriented, steep (>45°) escarpment (Figure 9a). The latter is 12.5 km long, up to 70 m high and has the morphology of connected 1.5-2 km wide scarps, giving it a “lacy” appearance. ROV imagery from this escarpment shows steep carbonate outcrops (Figure 9d). The seafloor between the northern wall of C4 and the escarpment shows an elongate, convex, mounding topography. The mound is up to 1.3 km wide and 20 m high (Figures 9c, 10). It has moderately steep sides (up to 6°) and is asymmetric in cross-section

(Figure 10). Along its northern boundary, the mound is characterised by numerous elongate and ellipsoidal depressions that are up to 50 m deep (Figure 9a). Three 90 m wide circular depressions, up to 13 m deep, are also observed in the central part of the mound. ROV imagery from across the surface of the mound shows gently sloping terrain covered by fine grained sediments and hosting a wide variety of bioturbation features.

FIGURE 10

The seismic signatures of the mound and escarpment are shown in Figure 10. The mound is up to 0.15 s (TWTT) thick and comprises packages of sub-parallel, convex-upward, high-amplitude reflectors of variable thicknesses (facies 2B). The base of this package is an irregular, stepped, semi-discontinuous reflector with highly variable amplitude. Below this reflector, the acoustic facies is transparent (facies 3). Along the northern boundary of the mound, the acoustically transparent facies has a steeply sloping (minimum of 25°, assuming P-wave velocity of 1600 m s^{-1}), southward facing edge that is up to 0.12 s (TWTT) high. This facies becomes exposed along the south-eastern boundary of the mound, where the seafloor is steepest and characterised by high backscatter (Figure 9a).

Other mounds, of a much smaller scale but similar morphology and seismic signature, occur along the top of the 12.5 km long escarpment and on the northern flank of channel C3 (Figure 5a).

4.1.4 Elongate ridge and adjacent seafloor

In the central part of the study area and upslope from the Cumecs Canyon head, a 7.5 km long ridge, up to 400 m wide and 30 m high, is located at a depth of 300-320 m (Figure 11a). The ridge is oriented N-S, parallel to the shelf edge, has steeply sloping sides (up to 40°) characterised by high backscatter, and is locally intersected by a 1.6 km wide amphitheatric scar (Figure 11a). At its southernmost edge, the ridge leads into a 3 km long and 30 m high escarpment sloping at ~7°. Further south, this ridge connects to a 3 km wide area of hummocky terrain.

FIGURE 11

Along its northern section, the topography of the ridge is undulating and divided in two by a depression (Figure 11a). Seismic reflection profiles crossing the ridge here show a strong, sloping and irregular reflector that very markedly divides the acoustic character of the ridge into an upper unit of sub-parallel, convex upward reflectors (facies 2B) and acoustically transparent facies (facies 3) below (Figure 11b). Either side of the ridge, the acoustically transparent facies appears vertically offset and downthrown by up to 0.25 s (TWTT) in the west and by 0.15 s (TWTT) in the east.

Seismic reflection profiles crossing the southern section of the ridge show it to be comprised of acoustically transparent facies (facies 3) that is vertically offset along the western flank (Figure 11c). Upslope of the ridge, the shallow stratigraphy consists of parallel to sub-parallel reflections (facies 2A) that can be sub-divided into two sub-facies on the basis of acoustic character and

geometry. The upper sub-facies (facies 2A-1) is 0.04 s (TWTT) thick at most, thinning eastwards and consisting of continuous, parallel, low to moderate amplitude reflectors that converge towards the ridge and shelf break. The lower sub-facies (facies 2A-2) generally consists of high to moderate amplitude and parallel reflector package that includes a number of clear, high amplitude, continuous reflectors. This sub-facies appears to have a relatively constant thickness, apart from where the underlying irregular surface is V-shaped; here, the sub-facies thickens as it appears to infill the topography, reaching a maximum thickness of 0.06 s (TWTT). In the easternmost section of the lower sub-facies and contiguous with the western flank of the ridge, there appears to be an offset in the sub-facies. This offset is associated with an abrupt change in the thickness of the seismic facies and the upward curvature of reflectors at a depth between 0.03 s and 0.06 s (TWTT) below the seafloor (Figure 11c). A similar offset can be observed further north (Figure 11d). On its eastern flank, the ridge is partially overlain by a sequence of convex-upward reflectors (facies 2B). To the west of this sequence is a moat-like depression (Figure 11c). The bathymetric data and all the seismic lines that cross the ridge show that this depression is present along the entire eastern flank of the ridge.

ROV imagery from across the ridge shows steep bedrock outcrops and carbonate hardgrounds (Figure 11e) that are occasionally covered by sessile megabenthos, particularly the anthipatharian *Leiopathes glaberrima* (Angeletti et al., 2015). Dredged material from the ROV site consists of carbonate hardgrounds (Figure 11f).

4.2 Gravity cores

4.2.1 Sedimentary facies

The nine sediment gravity cores have been obtained from channel C4 (CU12_05), the adjacent elongate mound (CU12_06) and upslope of the long escarpment (CU12_07), scar S2 (CU12_08 and CU12_09), adjacent undisturbed seafloor (CU12_10), upper Malta Escarpment scars (CU12_02 and CU12_03), and undisturbed seafloor upslope (CU12_01) (Figure 3). The sampled sediment is predominantly clay to silty clay of homogeneous lithology and physical properties. Five main sedimentary facies (A-E) are identified, with facies A, C and E being further subdivided into two sub-facies each (Figure 12):

i. Facies A1: olive grey, clayey mud with low foraminifera content, weakly bioturbated, and low P-wave velocity, gamma-ray density and magnetic susceptibility.
ii. Facies A2: similar to A1 in terms of physical properties, but darker colour (grey) mud with variable levels of bioturbation.
iii. Facies B: predominantly dark grey clayey mud with dispersed very fine sand and silt; devoid of foraminifera, with very high magnetic susceptibility, but same P-wave velocity and gamma-ray density as A1 and A2.
iv. Facies C1: sandy mud, abundant formanifera content, compacted with increased P-wave, gamma-ray density and magnetic susceptibility; no sedimentary structures, only some indistinct layering and slightly graded.

v. Facies C2: dark grey, silty mud with sandy patches (in some cores even sandier than C1), increased formaninifera content, ungraded to slightly graded, higher P-wave and gamma-ray density than C1.

vi. Facies D: light grey, highly compacted, formanifera-rich mud with shell fragments, with sharp upper boundary and gradational lower boundary; physical properties similar with A1, A2 and C but with distinctly higher lightness, making the layer easily identifiable in the cores where it is present.

vii. Facies E: greenish grey, clayey mud with rare foraminifera that is characterised by erratic variability of the physical properties, inclined (at 45^{o}) and sheared laminae and/or lighter olive grey clasts.

FIGURE 12

Textural and component analyses of the very fine sand and silt in facies B reveal the presence of scoria clasts and plagioclase crystals (Figure 13a), which indicate that it is a volcanic ash layer. The ash is dispersed in the clayey mud and does not form a distinct layer. We performed microprobe analyses of the glass matrix on samples of the very fine sand and silt material from 3 cores (CU12_01, CU12_07 and CU_10). Limited points for measurements were available because groundmass is largely devitrified. The results indicate that the tephra have Na-alkaline affinity (Na_2O 3.5-5.4 wt% > K_2O 2.3-4.3 wt%), and the Total Alkali Silica classification diagram (Figure 13b) shows mugearitic composition.

Figure 13

441

442 **4.2.2 AMS dates**

443

444 Four dates were acquired, two from CU12_01 and two from CU12_07. The two from CU12_01
445 bracket facies B at depths of 49 cm and 56 cm (Figure 12). The calibrated, reservoir corrected
446 ages we get for the two samples are 2140 – 2430 cal BP and 1850 – 2210 cal BP, respectively.
447 The two CU12_07 ages are from above and below facies C1 at depths of 123 cm and 203 cm,
448 respectively (Figure 12). The calibrated, reservoir corrected ages are 9740 – 10160 cal BP for the
449 123 cm sample and 44580 – 50000 cal BP for the 203 cm sample. The latter is at the age limit of
450 the technique and so the sediment may in fact be older.

451

452 **4.2.3 Core correlation**

453

454 Facies A is the most extensive facies, making up more than 80% of the total core recovered. The
455 facies used to correlate the cores are B (layer with high magnetic susceptibility peak because it
456 contains a tephra layer) and D (layer with characteristic lightness, colour and compaction)
457 (Figure 12). Facies D layer is not present in the cores in the north. There is a second high
458 magnetic susceptibility peak in cores CU12_01, CU12_10, CU12_08, CU12_06 and possibly
459 CU12_05, which is also used as a tie line for the correlation. The second high magnetic
460 susceptibly peak occurs about 25 cm below facies B. Facies C is found in all but two cores,
461 CU12_05 and CU12_08. Facies C layers correlate well and are found at the same stratigraphic
462 level downcore. What varies is the thickness of the beds. The grain size of facies C also varies
463 across the study area - it is coarsest in the north, particularly in CU12_07 and CU12_06, and finer

464 in the south. Core CU12_05 contains two layers of facies E – one above facies B and the other
465 one below. The only other core where facies E has been recorded is CU12_03.
466
467 **4.2.4 Shear strength measurements**
468
469 The shear strength measurements from the split cores (Figures 14a-d) were used to derive a
470 regression equation of the rate of change of shear strength with depth. Figure 14e shows a clear
471 trend of sediment strength increasing with depth at an average rate of 2.37 kPa m^{-1}.
472
473 FIGURE 14
474
475 **5. DISCUSSION**
476
477 **5.1 Stratigraphic framework**
478
479 The seismic stratigraphy across the study area is interpreted using published seismic profiles and
480 core/well data. Sequences of parallel and high amplitude reflectors (facies 2A) correspond to
481 conformable, stratified units of Plio-Pleistocene terrestrial, pelagic and hemipelagic sediments
482 (Max et al., 1993; Micallef et al., 2011; Osler and Algan, 1999; Tonarelli et al., 1993). These
483 Plio-Pleistocene sediments drape low reflectivity facies (facies 3), which have been interpreted as
484 carbonate bedrock sequences, the top of which corresponds to the Messinian Salinity Crisis
485 erosional surface (Bishop and Debono, 1996; Finetti, 1984; Lofi et al., 2011; Micallef et al.,
486 2011). This erosional surface is characteristically irregular and occasionally hosts wide

487 depressions. Where the Plio-Pleistocene sediment drape is thin, the seafloor topography is
488 hummocky because it traces the underlying erosional surface.
489
490 The Plio-Pleistocene sedimentary sequence is characterised by a number of high amplitude
491 reflectors, likely the result of alternating depositional and erosional processes related to glacio-
492 eustatic oscillations. Because of its widespread distribution and depth of occurrence (seafloor
493 shallower than 140 m), as well as its resemblance to similarly interpreted features in the central
494 Mediterranean, we identify the most widespread and distinctive unconformity (unconformity 1;
495 Figure 4b) as a sequence boundary formed by subaerial erosion during sea level fall associated
496 with the Last Glacial Maximum (LGM) (Lambeck et al., 2011; Martorelli et al., 2010). The
497 acoustically transparent material on top of the sequence boundary (facies 1) is thus interpreted as
498 a transgressive systems tract of post-LGM deposition.
499
500 The gravity cores inform us about the shallow stratigraphy of the last 50-60 ka.
501
502 The chemical and component analyses of the tephra material in facies B indicate that the tephra
503 deposit in all the studies cores is the same, thus allowing internal stratigraphic correlations.
504 Furthermore, these data show that its composition is in agreement with Etna volcanics (Corsaro
505 and Pompilio, 2004), and that it can be correlated with those associated with a well-known
506 historical Plinian eruption produced by Etna in 122 BC (Coltelli et al., 1998) (Figure 13b).
507
508 The most prevalent facies, A1 and A2, are interpreted as hemipelagites. The ages obtained from
509 CU12_01 indicate an age reversal. On the basis of the volcanological determination of the ash

510 layer matching the 122 BC (2072 BP) Etna eruption, we are fairly confident that the 56 cm
511 sample 1850 – 2210 cal BP age is more reliable. We attribute the shallower but older age to
512 potential sampling of older sediment in a bioturbated interval. Using this age, the sedimentation
513 rate for facies A1 is estimated at 11.8 cm ka^{-1}; it is not possible to estimate a sedimentation rate
514 for facies A2 with the available data. The different characteristics of facies A1 and A2 likely
515 reflect different amounts of primary productivity, climate effects and water mass changes.
516
517 In view of the absence of terrigenous sources of sand and the oceanographic context in which the
518 deposits are found, Facies C is interpreted to represent contourites. The different characteristics
519 of C1 and C2 possibly reflect changes in bottom current activity, either over time or across the
520 slope. The sedimentation rate of the contourites is estimated based on the dates of CU12_07 at
521 2.6 cm ka^{-1}, which is a lot slower than hemipelagic sedimentation, likely reflecting the alternating
522 erosional and depositional processes that take place during contourite formation (Masson et al.,
523 2010).
524
525 Facies D is difficult to interpret - it is either a hemipelagite, reflecting a brief period of very high
526 productivity, or a debrite. Based on its limited and restricted distribution on the Malta Plateau, we
527 favour the first interpretation and suggest that this layer represents a brief period of high
528 carbonate productivity. Through correlation of cores CU12_10, 09 and 01 with CU12_07, we
529 estimate the minimum age of this layer at around 50 ka BP. This could place the formation of the
530 layer in early Marine Isotope Stage (MIS) 3, which was characterised by abrupt climatic changes
531 (Siddall et al., 2008).
532

533 The characteristics of facies E, with the inclined and deformed layers and the interspersed clasts
534 of different lithologies, suggest that they are debrites. Cores recording such facies are found
535 within scars (CU12_03) or the axis of channel C4 (CU12_05), but not in undisturbed seafloor,
536 which corroborates our interpretation.
537
538 **5.2 Seafloor geomorphic processes**
539
540 The seafloor in the eastern Malta Plateau has been shaped by three main processes (Figure 5b):
541
542 **5.2.1 Mass movements**
543
544 **5.2.1.1 Nature of mass movements**
545
546 We interpret the scars documented across the study area as evidence of slope instability. Mass
547 movements are concentrated along the shelf break and channel C4. They extend over three orders
548 of magnitude (in terms of area) and entail three styles of deformation:
549
550 (i) The linear to arcuate steep headwalls, and the smooth and planar scars and slip
551 surfaces, indicate that the majority of the mass movements appear to be translational
552 in nature (*sensu* Locat and Lee (2002));
553 (ii) Both the repetitive pattern of ridges and troughs observed in scars S2 and S3 and in
554 the upslope sections of some of the smaller scars, and the partial deformation of a
555 sedimentary package (facies 2C) above a planar sedimentary layer, are characteristic

of submarine spreading (Micallef et al., 2007b). Spreading involves the extension of a sediment unit and its break up into blocks that slide above a planar slip surface.

(iii) The material in the scars has undergone internal deformation to varying degrees, as indicated by the chaotic seismic signatures (facies 2D) of mass movement deposits (Figure 8b). This is likely caused by increased plastic deformation due to the evolution of translational slides into debris flows, particularly across abrupt seafloor gradient changes that can cause flow transformation in mass movements (e.g. Georgiopoulou et al., 2010; Piper et al., 1999). This process is corroborated by the occurrence of debrites in cores located downslope of some slide scars (e.g. CU12_05).

The mass movements appear to have generally been very mobile, as all the material appears to have been evacuated from most scars, apart from S2 and S3. When compared to the undisturbed seafloor around the scars, it is clear that the material being mobilised is primarily very gently sloping, stratified Plio-Pleistocene hemipelagic mud.

5.2.1.2 Timing of mass movements

Most of the scars' headwalls and sidewalls have smooth edges, whilst all the scars crossed by seismic reflection profiles appear covered by a hemipelagic drape. This indicates that the mass movements are not recent events. Two debrites have been recorded in the axis of channel C4. The more recent debrite is younger than the 122 BC Etna eruption, whereas the older debrite has an age of ~17 ka (based on a sedimentation rate of 11.8 cm ka^{-1}). The debrite at the bottom of core

578 CU12_03 (upper Malta Escarpment slide scar) is older than this event. This suggests that
579 different parts of the eastern Malta Plateau were unstable at different times.
580
581 **5.2.1.3 Pre-conditioning factors and triggering mechanisms of mass movements**
582
583 As the mass movements appear to have detached along glide planes parallel to the stratigraphy,
584 we conclude that they are stratigraphically-controlled. The planar slip surface coincides with
585 specific stratigraphic layers that are locally shared by different slope failure events. It is clear that
586 a specific sedimentary layer (or layers) has acted as a weak layer, yet it is difficult to determine
587 the nature of the slip surfaces and why they were prone to failure.
588
589 In the upper Malta Escarpment slide scar (S5; Figure 8), the stratigraphic position of the ~17 ka
590 old debrite (facies E) coincides with the stratigraphic position where the light-coloured and
591 compact layer was expected (facies D). The base of the debrite was not sampled by core
592 CU12_03, but in core CU12_02 we find a thin sandy layer. The sequence below it does not
593 correlate with the sequence in the equivalent stratigraphic depth in core CU12_01, and the
594 gamma-ray density log suggests that this sequence is denser than other cores at this depth
595 downcore. We interpret this to indicate that the thin sandy layer in core CU12_02 is a thin
596 turbidite deposit on an erosional surface. This was likely generated by the passage of a debris
597 flow that left no debrite deposit in the location of CU12_02; however, a thin turbidite could have
598 been deposited by either an accompanying turbidity current or by local flow transformation of the
599 debris flow into more dilute conditions. It is unknown how deep the debris flow eroded, but the
600 gamma-ray density measurements suggest that this sequence belongs to a much deeper

601 stratigraphic unit that has been subjected to higher compaction. The light-coloured compact layer
602 (facies D) is missing in core CU12_03, either because it lies below the debrite and the core did
603 not reach it, or it was incorporated in the slope failure. It is likely, given its contrasting properties
604 to the surrounding hemipelagic material, that it formed the weak layer for the slide. The
605 difference from the encasing hemipelagic mud, in terms of geotechnical properties, has the
606 potential to generate a strength contrast and provide a potential focus for a rupture surface (Locat
607 et al., 2014). It is not clear whether differences in geotechnical properties between volcanic ash
608 layers and hemipelagic mud could also have led to the development of a weak layer. On one
609 hand, ash layers have been shown to promote translational sliding due to compaction and
610 overpressure generation during large earthquakes, as demonstrated offshore Central America
611 (Harders et al., 2010). On the contrary, others have shown that volcanic ash needs to be strongly
612 altered to facilitate slope failure, and this process tends to take place at considerable depths (>800
613 m) below the seafloor (Wiemer and Kopf, 2015).
614
615 Sediment loading and associated excess pore pressure development are not considered a key
616 preconditioning factor in the eastern Malta Plateau, in view of the low sedimentation rates
617 recorded in our cores and reported in the literature (Max et al., 1993; Osler and Algan, 1999).
618 Excess pore pressure may also be induced by fluid flow. Deep fluid flow systems, sourced by
619 Late Mesozoic sedimentary units and transferred via faults in Cenozoic carbonate sequences,
620 have been documented in parts of the eastern Malta Plateau (Micallef et al., 2011). The 90 m
621 wide, circular depressions identified on the elongate mound of channel C4 may be pockmarks,
622 and thus evidence of fluid flow and escape at the seafloor. However, such evidence is not
623 extensive across the study area and further investigation would be needed to determine whether

624 the flow rates and characteristics of the fluid are adequate to precondition parts of the eastern
625 Malta Plateau seafloor to failure.
626
627 We propose two potential triggers of slope instability across the eastern Malta Plateau. The mass
628 movements display three levels of retrogression and are located upslope of other mass
629 movements, channels, canyons or escarpments. These indicate that loss of support plays a key
630 role in triggering slope instability in the study area. Processes shaping the seafloor in the upper
631 Malta Escarpment – canyon erosion and associated slope failures – have been particularly
632 important in this regard. We consider channels C5 and C6 as erosive channels developed by the
633 upslope retrogression of heads of canyons incising the Malta Escarpment that could have
634 potentially triggered slope failure in scars S2 and S4. The second trigger is seismicity. Although
635 recent seismic activity has mostly been restricted to the northern section of the Malta Escarpment
636 (Argnani and Bonazzi, 2005), ground shaking associated with distal earthquakes could still have
637 played a role in triggering slope instability across the study area.
638
639 **5.2.1.4 Seismic activity as a potential trigger of mass movements**
640
641 We use slope stability modelling to explore the hypothesis that large and infrequent seismic
642 ground shaking events are responsible for triggering mass movements in the eastern Malta
643 Plateau. Our stability model is based on the mass movement associated with scar S2 because it is
644 the major slope instability feature that has been sampled in our study area. We model the stability
645 of the intact slope sediments by drawing on information from seismic reflection data by
646 developing a composite bathymetric profile in the downslope direction of failure. Long profile

geometry and Sparker profile 9 indicate that failure occurred at a depth of 80 m below the seafloor (using a P-wave velocity of 1600 m s^{-1} for depth conversion). Since most of the landslides are stratigraphically-controlled translational failures, we define the failure surface at 80 m below and parallel to the seafloor. We assume a free face on the downslope boundary of the slope model, as observed on the intact shelf edge.

A static limit equilibrium slope stability model based on this planar failure model, the material strength parameters derived from shear vane testing (Figure 14) and the Bishop methods of slices (implemented in Rocscience software SLIDE 5.0) results in a factor of safety (Fs) = 3.3. A Fs = 1.0 signifies a slope in equilibrium and any Fs > 1.0 indicates that under present conditions the slope is stable (unfailed). In the case where Fs > 1.0, an external perturbation is required for failure to occur (e.g. ground shaking due to earthquakes).

To assess the potential for earthquake-related failure, a horizontal earthquake load is considered in the model. A range of values for the horizontal seismic coefficient are trialed to assess the stability of the slope. The horizontal seismic coefficient represents a horizontal seismic force directed out of the slope (i.e. in the direction of failure). The seismic coefficient is a dimensionless coefficient that represents the (maximum) earthquake acceleration as a fraction of the acceleration due to gravity. This is related to Peak Ground Acceleration (PGA), which is often used to model earthquake energy for submarine landslides but is immediately comparable. Seed and Idriss (1971) suggest applying an empirical dampening relationship to the seismic coefficient derived from pseudo-static stability modelling to make it comparable with PGA values (Strozyk et al., 2010). Testing a range of seismic coefficient values indicates that a seismic

load of 0.085g (where g is the acceleration due to Earth's gravity) is required to reduce the stability of the slope to unity or Fs = 1.0 (Figure 15a). Applying the empirical dampening relationship of Seed and Idriss (1971) delivers an equivalent PGA value of 0.13g. To assess the time period over which this level of ground acceleration could be generated, a probabilistic seismic hazard curve was compiled for the site (Figure 15b). This model indicates that the required PGA would be exceeded at a Return Interval of just less than 1500 years. By taking into consideration seismic monitoring and hazard assessments of the Maltese Islands and central Mediterranean Sea, it appears that only ground shaking associated with distal earthquakes of EMS-98 intensities >VIII has the potential of triggering slope failures in eastern Malta Plateau at present (Agius and Galea, 2011; Amato and Mele, 2008; Galea, 2007). During the Plio-Pleistocene, the sources of earthquakes may have been more proximal to the seafloor affected by slope instability, and the earthquake recurrence intervals could have been lower, in view of the more widespread strike-slip fault activity upslope of the Cumecs Canyon during this period (see section 5.2.2).

FIGURE 15

5.2.2 Faulting

We interpret the northern channels (C1-C4) as structurally-controlled channels. They consist of a drape of stratified Plio-Pleistocene hemipelagic sedimentary sequences that traces the underlying carbonate basement, which has been shaped into an irregular and stepped topography by subaerial erosion during the Messinian Salinity Crisis and normal faulting, respectively. Most

693 fault scarps have been buried, except where the fault scarp was very steep (e.g. eastern part of the
694 northern wall of C4); the latter may indicate that the fault is still active and displacement has
695 occurred recently in this region. The orientation of the faults is not consistent, varying from NW-
696 SE in the north, to W-E in the south. Vertical displacement reaches up to 170 m (as in the case of
697 the elongate mound north of C4). The channels and associated faults define the boundaries of a
698 horst and graben system in the central part of the study area (Figure 5b). Lack of offset seismic
699 reflectors above the Messinian low-stand erosional surface in our seismic reflection data indicates
700 that the system appears to have been inactive since the Messinian Salinity Crisis. Evidence of
701 channel erosion across the seabed is lacking, apart from small mass movements across the walls
702 of the largest channel.
703
704 The N-S oriented elongate ridge located upslope from the Cumecs Canyon is interpreted as a
705 horst block, resulting from either antithetic normal faulting or vertical uplift associated with
706 transpressive strike-slip faulting. Erosion of the central section of the ridge by a large slope
707 failure scar indicates that the formation of the horst predates the latest development of the upper
708 Malta Escarpment canyons further east. Offset and convex-upward horizons in the Plio-
709 Pleistocene sedimentary cover in the eastern Malta Plateau, adjacent to the southern section of the
710 ridge (Figure 11c,d), are indicative of transpressive deformation due to strike-slip faulting. No
711 displacement appears to have occurred along these faults in recent times, in agreement with
712 Argnani and Bonazzi (2005) and the lack of recent seismic activity along the Malta Escarpment
713 (Agius and Galea, 2011; Amato and Mele, 2008).
714

715 The NW-SE and N-S faults across the eastern Malta Plateau share a similar orientation with a
716 number of known faults in the area (Figure 1). The described fault system is also extremely
717 similar to that documented along eastern Sicily further north (Adam et al., 2000; Argnani and
718 Bonazzi, 2005; Grasso, 1993). Between Augusta and Siracusa, NW-SE oriented extensional
719 grabens have developed in association with NNW-SSE-trending sinistral strike-slip fault activity.
720 Transpression associated with the latter is responsible for the topographic highs of the Monte
721 Tauro, Santa Panagia and Maddalena Horsts. In view of this similarity, we infer that the tectonic
722 context for all these faults systems is the same.
723
724 An alternative explanation for the N-S oriented elongate ridge is that it has a biogenic origin. It is
725 morphologically similar to deep-water mounded carbonate structures, which have been described
726 offshore NW Europe and Florida and interpreted as resulting from in situ deep-water coral
727 growth, sediment build up and cementation (e.g. (Dorschel et al., 2005; Freiwald et al., 1997;
728 Paull et al., 2000; Wheeler et al., 2007). However, such structures are generally located in water
729 depths exceeding 500 m and the base of the coral growth is visible on the seismic reflection
730 profiles. Neither of these characteristics is shared by the elongate ridge on the eastern Malta
731 Plateau.
732
733 **5.2.3 Bottom currents**
734
735 The morphology and seismic signature (facies 2B) of the elongate mounds are typical of
736 mounded contouritic drifts (Rebesco and Stow, 2001; Stow et al., 2002). The depressions
737 contiguous to the drifts are thus interpreted as moats. The contouritic drifts are likely the result of

738 the interaction of bottom currents with the topography created by faults (structurally-controlled
739 channels, horst blocks). Bottom current flows may have also played a role in channel incision –
740 in fact, the core taken from the axis of channel C4 (CU12_05) is devoid of contourites. The
741 bottom currents responsible for the development of the contourites must have been stronger
742 across the longest mound in the north, and weaker across the small mounds in the south, as
743 evidenced by the differences in the thickness of the contourite layers and grain size in cores
744 CU12_07 and CU12_01.
745
746 Our interpretation is corroborated by the occurrence of contourite layers in sediment cores
747 (Figure 12). It appears that during MIS 2 and 3, bottom currents were active in the area of
748 channel C4 and the associated mound area, but their sedimentation was slow. Based on the
749 difference in accumulation rates between the contourites and the hemipelagites, we infer that the
750 contouritic drift along the northern wall of the channel C4 contains surfaces of erosion and non-
751 deposition, and/or that the finer sediment was winnowed and the contouritic sediment was
752 continuously reworked. The latter scenario is supported by the sandier nature of facies C in
753 comparison to facies A. In view of all this, it would be wrong to assume that contouritic
754 deposition started 45 ka ago, as the base might be erosional too. What we can say with some
755 confidence is that contourite deposition subsided around 9740 BP. It is likely that the bottom
756 currents building contourites either ceased to flow or shifted position, because their effect is no
757 longer captured in the cores. This change may be associated with post-LGM sea level rise and a
758 resulting increase in sedimentation in the area, which is anticipated in carbonate producing
759 regions (Schlager et al., 1994).
760

761 The location of these deposits allows us to infer long-term flow of benthic currents both
762 perpendicular and parallel to the Malta Escarpment. The bottom currents responsible for these
763 deposits may be associated with either Modified Atlantic Water flows during sea level lowstands
764 or Levantine Intermediate Water flows at present (Millot, 2005). In the present day, the action of
765 bottom currents in proximity of the southern mounds is confirmed by the occurrence of
766 suspension feeders, such as anthipatharian assemblages (Angeletti et al., 2015). We think that the
767 contouritic drifts, particularly those in channel C4, provide an excellent record of
768 palaeoceanographic variability in the Sicily Channel since the Messinian Salinity Crisis, and are
769 therefore worth sampling and analysing in detail.
770
771 **6. CONCLUSIONS**
772
773 Analyses of geophysical, sedimentological and visual data from the eastern Malta Plateau, central
774 Mediterranean Sea, have shown that the outer shelf of a submarine carbonate escarpment bears
775 evidence of widespread geologic and geomorphic activity, most of which is directly linked to
776 escarpment-forming processes. The smooth and gently sloping seafloor of the eastern Malta
777 Plateau hosts forty eight erosional scars (up to 70 km^2 in area), six channels (up to 12 km in
778 length) and numerous smaller-scale channels, three elongate mounds (up to 12.5 km in length),
779 and an elongate ridge (7.5 km in length) across an area of 650 km^2. We propose three key
780 processes to explain the origin of these morphologies:
781
782 (i) Mass movements - in the form of translational slides, spreading and debris flows –
783 that mobilised stratified Plio-Pleistocene hemipelagic mud. These retrogressive mass

movements extend over three orders of magnitude, cluster along the shelf break, and the majority are not recent events. Loss of support, due to canyon erosion and associated slope failures in the upper Malta Escarpment, and seismicity are the most plausible triggers.

(ii) The development of NW-SE oriented extensional grabens and a NNW-SSE oriented horst in association with NNW-SSE trending sinistral strike-slip deformation in Cenozoic carbonates. The tectonic framework responsible for this deformation entailed the development of a mega-hinge fault system along the Malta Escarpment since the Late Mesozoic, and SE-NW directed horizontal shortening since the Late Miocene. The faults associated with such deformation were active up to the Plio-Pleistocene.

(iii) Sediment erosion and deposition by bottom currents - either Modified Atlantic Water flows during sea level lowstands or Levantine Intermediate Water flows at present – flowing perpendicular and parallel to Malta Escarpment was responsible for the development of contouritic drifts and channels.

Outer shelves comprise an important yet neglected element in the overall evolution of carbonate escarpments. A more comprehensive investigation of such settings is thus warranted, also in terms of the hazard they pose to nearby coastal communities and seafloor infrastructures, as well their value as archives of palaeo-environmental change.

7. ACKNOWLEDGEMENTS

807 This research was undertaken with funding from Marie Curie Career Integration Grant PCIG13-
808 GA-2013-618149 (SCARP), Marie Curie Intra-European Fellowship PIEF-GA-2009-252702
809 (CAGE), ERC Starting Grant n°258482 (CODEMAP) and collaborative project n°228344
810 (EUROFLEETS), all within the 7th European Community Framework Programme. Financial
811 support was also provided by a University of Malta Research Grant, the Royal Society of New
812 Zealand (through the International Mobility Fund), Crown Research Institute Core funding to
813 NIWA, and the Griffith Geoscience Awards (Department of Communications, Energy and
814 Natural Resources under the National Geoscience Programme 2007–2013 of Ireland). We are
815 indebted to the CUMECS and CUMECS-2 shipboard parties, captains, crew and technicians on
816 board the R/V Urania and R/V OGS Explora for their assistance during data collection. We also
817 thank Gareth Crutchley, Luis Pinheiro and Susi Woelz for their assistance with seismic data
818 processing, Suzanne Maclachlan and Jeremy Sothcott for their help with core analyses, and
819 Andrea Orlando and Eleonora Braschi for assistance with microprobe analyses. We are grateful
820 to Deniz Cukur and an anonymous reviewer for their insightful reviews. The oceanographic
821 surveys were possible following permits issued by the Italian and Maltese authorities.
822

823 **8. REFERENCES**

824

825 Adam, J., Reuther, C.D., Grasso, M., Torelli, L., 2000. Active fault kinematics and crustal
826 stresses along the Ionian margin of southeastern Sicily. Tectonophysics 326, 217-239.
827 Agius, M.R., Galea, P., 2011. A single-station automated earthquake location system at Wied
828 Dalam station. Seismological Research Letters 82, 545-559.

829 Amato, A., Mele, F.M., 2008. Performance of the INGV National Seismic Network from 1997 to
830 2007. Annalys of Geophysics 51, 417-431.
831 Angeletti, L., Mecho, A., Doya, C., Micallef, A., Huvenne, V., Georgiopoulou, A., Taviani, M.,
832 2015. First report of live deep-water cnidarian assemblages from the Malta Escarpment. Italian
833 Journal of Zoology 8, 291-297.
834 Argnani, A., Bonazzi, C., 2005. Malta Escarpment fault zone offshore eastern Sicily: Pliocene-
835 Quaternary tectonic evolution based on new multichannel seismic data. Tectonics 24, TC4009.
836 Ben-Avraham, Z., Grasso, M., 1991. Crustal structure variations and transcurrent faulting at the
837 eastern and western margins of the eastern Mediterranean. Tectonophysics 196, 269-277.
838 Béranger, K., Mortier, L., Gasparini, G.P., Gervasio, L., Astraldi, M., Crépon, M., 2004. The
839 dynamics of the Sicily Strait: A comprehensive study from observations and models. Deep-Sea
840 Research 51, 411-440.
841 Bishop, W.F., Debono, G., 1996. The hydrocarbon geology of southern offshore Malta and
842 surrounding regions. Journal of Petroleum Geology 19, 129-160.
843 Brooks, G.R., Doyle, L.J., McNeillie, J.I., 1986. A massive carbonate gravity-flow intercalated in
844 the Lower Mississippi Fan. Initial Reports of the Deep Sea Drilling Project 96, 541-546.
845 Casero, P., Cita, M.B., Croce, M., De Micheli, A., 1984. Tentative di interpretazione evolutiva
846 della scarpata di Malta basata su dati geologici e geofisici. Memorie della Societa` Geologica
847 Italiana 27, 233-253.
848 Catalano, R., Doglioni, C., Merlini, S., 2000a. On the Mesozoic Ionian Basin. Geophysical
849 Journal International 143, 1-24.

850 Catalano, R., Franchino, A., Merlini, S., Sulli, A., 2000b. A crustal section from Eastern Algerian
851 basin to the Ionian ocean (Central Mediterranean). Memorie della Societa` Geologica Italiana 55,
852 71-85.
853 Catalano, R., Sulli, A., 2006. Crustal image of the Ionian basin and accretionary wedge.
854 Bollettino di Geofisica Teorica ed Applicata 47, 343-374.
855 Ciappa, A.C., 2009. Surface circulation patterns in the Sicily Channel and Ionian Sea as revealed
856 by MODIS chlorophyll images from 2003 to 2007. Continental Shelf Research 29, 2099-2109.
857 Cita, M.B., Benelli, F., Bigioggero, B., Chezar, H., Colombo, A., Fantini Sestini, N., Freeman-
858 Lynde, R.P., Iaccarino, S., Jadoul, F., Legnani, E., Malinverno, A., Massiotta, P., Paggi, L.,
859 Premoli Silva, I., 1980. Contribution to the geological exploration of the Malta Escarpment
860 (eastern Mediterranean). Rivista Italiana di Paleontologia e Stratigrafia 86, 316-356.
861 Coltelli, M., Del Carlo, P., Vezzoli, L., 1998. The discovery of a Plinian basaltic eruption of
862 Roman age at Mt. Etna. Geology 26, 1095-1098.
863 Commeau, R.F., Paull, C.K., Commeau, J.A., Poppe, L.J., 1987. Chemistry and mineralogy of
864 pyrite-enriched sediments at a passive margin sulfide brine seep: abyssal Gulf of Mexico. Earth
865 and Planetary Science Letters 82, 62-74.
866 Corsaro, R.A., Pompilio, M., 2004. Buoyancy-controlled eruption of magmas at Mt Etna. Terra
867 Nova 16, 16-22.
868 De Martini, P.M., Barbano, M.S., Smedile, A., Gerardi, F., Pantosti, D., Del Carlo, P., Pirrotta,
869 C., 2010. A 4000 yrs long record of tsunami deposits along the coast of the Augusta Bay (eastern
870 Sicily, Italy): Paleoseismological implications. Marine Geology 276, 42-57.

871 Dillon, W.P., Valentine, P.C., Paull, C.K., 1987. The Blake Escarpment - A product of erosional
872 processes in the deep ocean, in: Cooper, R. (Ed.), Symposium Series for Undersea Research.
873 National Oceanic and Atmospheric Administration, Washington, D.C., pp. 177-190.
874 Dorschel, B., Hebbeln, D., Rüggeberg, A., Dullo, W.-C., Freiwald, A., 2005. Growth and erosion
875 of a cold-water coral covered carbonate mound in the Northeast Atlantic during the Late
876 Pleistocene and Holocene. Earth and Planetary Science Letters 233, 33-44.
877 Finetti, I., 1982. Structure, stratigraphy and evolution of the central Mediterranean. Bollettino di
878 Geofisica Teorica e Applicata 24, 274-315.
879 Finetti, I., 1984. Geophysical study of the Sicily Channel Zone. Bollettino di Geofisica Teorica
880 ed Applicata 26, 3-28.
881 Freeman-Lynde, R.P., Cita, M.B., Jadoul, F., Miller, E.L., Ryan, W.B.F., 1981. Marine geology
882 of the Bahama Escarpment. Marine Geology 44, 119-156.
883 Freiwald, A., Henrich, R., Patzold, J., 1997. Anatomy of a deep-water coral reef mound, Norway,
884 in: James, N.P., Clarke, J.A.D. (Eds.), Cool-Water Carbonates. Society of Sedimentary Geology
885 Special Publication, pp. 141-162.
886 Galea, P., 2007. Seismic history of the Maltese Islands and considerations on seismic risk.
887 Annals of Geophysics 50, 725-740.
888 Gardiner, W., Grasso, M., Sedgeley, D., 1995. Plio-Pleistocene fault movement as evidence for
889 mega-block kinematics within the Hyblean-Malta Plateau, Central Mediterranean. Journal of
890 Geodynamics 19, 35-51.
891 Georgiopoulou, A., Masson, D.G., Wynn, R.B., Krastel, S., 2010. Sahara Slide: Age, initiation
892 and processes of a giant submarine slide. Geochemistry, Geophysics, Geosystems 11, Q07014.

893 Grasso, M., 1993. Pleistocene structures along the Ionian side of the Hyblean Plateau (SE Sicily):
894 Implications for the tectonic evolution of the Malta Escarpment, in: Max, M.D., Colantoni, P.
895 (Eds.), Geological Development of the Sicilian-Tunisian Platform. UNESCO, Urbino, pp. 49-54.
896 Gutscher, M.-A., Dominguez, S., de Lepinay, B.M., Pinheiro, L., Gallais, F., Babonneau, N.,
897 Cattaneo, A., Le Faou, Y., Barreca, G., Micallef, A., Rovere, M., 2016. Tectonic expression of an
898 active slab tear from high-resolution seismic and bathymetric data offshore Sicily (Ionian Sea).
899 Tectonics 35, 39-54.
900 Halley, R.B., Schlager, W., 1983. Alternative diagenetic models for Cretaceous talus deposits,
901 Deep Sea Drilling Project Site 536, Gulf of Mexico, in: Buffler, R.T., Schlager, W. (Eds.), Initial
902 Reports of the Deep-Sea Drilling Project, Leg 77. U.S. Government Printing Office, Washington,
903 D.C., pp. 397-408.
904 Harders, R., Kutterolf, S., Hensen, C., Moerz, T., Brueckmann, W., 2010. Tephra layers: A
905 controlling factor on submarine translational sliding? Geochemistry, Geophysics, Geosystems 11,
906 Q05S23.
907 Holland, C.W., Etiope, G., Milkov, A.V., Michelozzi, E., Favali, P., 2003. Mud volcanoes
908 discovered offshore Sicily. Marine Geology 199, 1-6.
909 Jongsma, D., Van Hinte, J.E., Woodside, J.M., 1985. Geologic structure and neotectonics of the
910 north African continental margin south of Sicily. Marine and Petroleum Geology 2, 156-177.
911 Lambeck, K., Antonioli, F., Anzidei, M., Ferranti, L., Leoni, G., Silenzi, S., 2011. Sea level
912 change along the Italian coasts during Holocene and prediction for the future. Quaternary
913 International 232, 250-257.
914 Land, L.A., Paull, C.K., Spiess, F.N., 1999. Abyssal erosion and scarp retreat: Deep Tow
915 observations of the Blake Escarpment and Blake Spur. Marine Geology 160, 63-83.

916 Le Bas, M.J., Le Maitre, R.W., Streckeisen, A., Zanettin, B.A., 1986. Chemical classification of
917 volcanic rocks based on the total alkali-silica diagram. Journal of Petrology, 745-750.
918 Le Bas, T.P., Hühnerbach, V., 1998. PRISM Processing of remotely-sensed imagery for seafloor
919 mapping handbook. Southampton Oceanography Centre, p. 82.
920 Lermusiaux, P.F.J., Robinson, A.R., 2001. Features of dominant mesoscale variability,
921 circulation patterns and dynamics in the Strait of Sicily. Deep-Sea Research I Oceanographic
922 Research Paper 48, 1953-1997.
923 Lipparini, L., Scrocca, D., Marisili, P., Morandi, S., 2009. Offshore Malta licence in the Central
924 Mediterranean Sea offers hope of hydrocarbon potential. First Break 27, 105-116.
925 Locat, J., Lee, H.J., 2002. Submarine landslides: advances and challenges. Canadian
926 Geotechnical Journal 39, 191-212.
927 Locat, J., Leroueil, S., Locat, A., Lee, H.J., 2014. Weak yayers: Their definition and
928 classification from a geotechnical perspective, in: Krastel, S., Berhmann, J.H., Volker, D., Stipp,
929 M., Berndt, C., Urgeles, R., Chaytor, J.D., Huhn, K., Strasser, M., Harbitz, C.B. (Eds.),
930 Submarine Mass Movements and Their Consequences. Springer International Publishing,
931 Switzerland, pp. 3-12.
932 Lofi, J., Deverchere, J., Gaullier, V., Gillet, H., Gorini, C., Guennoc, P., Loncke, L., Maillard, A.,
933 Sage, F., Thinon, I., 2011. Seismic Atlas of The "Messinian Salinity Crisis" markers in the
934 Mediterranean and Black Seas. Commission de la carte géologique du monde et société
935 géologique de France.
936 Lowe, D.J., 2011. Tephrochronology and its application: A review. Quaternary Geochronology 6.

937 Martorelli, E., Chiocci, F., Orlando, L., 2010. Imaging continental shelf shallow stratigraphy by
938 using different high-resolution seismic sources: An example from the Calabro-Tyrrhenian margin
939 (Mediterranean Sea). Brazilian Journal of Oceanography 58, 55-66.
940 Masson, D.G., Plets, R.M.K., Huvenne, V.A.I., Wynn, R.B., Bett, B.J., 2010. Sedimentology and
941 depositional history of Holocene sandy contourites on the lower slope of the Faroe-Shetland
942 Channel, northwest of the UK. Marine Geology 268, 85-96.
943 Max, M.D., Kristensen, A., Michelozzi, E., 1993. Small scale Plio-Quaternary sequence
944 stratigraphy and shallow geology of the west-central Malta Plateau, in: Max, M.D., Colantoni, P.
945 (Eds.), Geological Development of the Sicilian-Tunisian Platform. UNESCO, Urbino, pp. 117-
946 122.
947 Micallef, A., Berndt, C., Debono, G., 2011. Fluid flow systems of the Malta Plateau, Central
948 Mediterranean Sea. Marine Geology 284, 74-85.
949 Micallef, A., Berndt, C., Masson, D.G., Stow, D.A.V., 2007a. A technique for the morphological
950 characterization of submarine landscapes as exemplified by debris flows of the Storegga Slide.
951 Journal of Geophysical Research 112, F02001.
952 Micallef, A., Gutscher, M.A., Georgiopoulou, A., Mountjoy, J., Lo Iacono, C., Paull, C.K., Le
953 Bas, T., Huvenne, V.A.I., Accettella, D., in review. Morphology and origin of a 3000-m high
954 carbonate escarpment: The central Malta Escarpment, Mediterranean Sea. Geomorphology.
955 Micallef, A., Masson, D.G., Berndt, C., Stow, D.A.V., 2007b. Morphology and mechanics of
956 submarine spreading: A case study from the Storegga Slide. Journal of Geophysical Research
957 112, F03023.
958 Millot, C., 2005. Circulation in the Mediterranean Sea: Evidences, debates and unanswered
959 questions. Scientia Marina 69, 5-21.

960 Millot, C., Taupier-Letage, I., 2005. Circulation in the Mediterranean Sea, The Handbook of
961 Environmental Chemistry. Springer, Berlin/Heidelberg, pp. 29-66.
962 Mullins, H.T., Gardulski, A.F., Hine, A.C., 1986. Catastrophic collapse of the west Florida
963 carbonate platform margin. Geology 14, 167-170.
964 Nicolich, R., Laigle, M., Hirn, A., Cernobori, L., Gallart, J., 2000. Crustal structure of the Ionian
965 margin of Sicily: Etna volcano in the frame of regional evolution. Tectonophysics 329, 121-139.
966 Osler, J., Algan, O., 1999. A high resolution seismic sequence analysis of the Malta Plateau,
967 Saclantcen Report.
968 Paull, C.K., Caress, D.W., Gwiazda, R., Urrutia-Fucugauchi, J., Rebolledo-Vieyra, M., Lundsten,
969 E., Anderson, K., Sumner, E.J., 2014. Cretaceous–Paleogene boundary exposed: Campeche
970 Escarpment, Gulf of Mexico. Marine Geology 357, 392-400.
971 Paull, C.K., Chanton, J.P., Neumann, A.C., Coston, J.A., Martens, C.S., 1992. Indicators of
972 methane-derived carbonates and chemosynthetic organic carbon deposits: Examples from the
973 Florida Escarpment. Palaios 7, 361-375.
974 Paull, C.K., Dillon, W.P., 1980. Erosional origin of the Blake Escarpment: An alternative
975 hypothesis. Geology 8, 538-542.
976 Paull, C.K., Freeman-Lynde, R.P., Bralower, T.J., Gardemal, J.M., Neumann, A.C., D'Argenio,
977 B., Marsella, E., 1990. Geology of the strata exposed on the Florida Escarpment. Marine Geology
978 91, 177-194.
979 Paull, C.K., Neumann, A.C., 1987. Continental margin brine seeps: Their geological
980 consequences. Geology 15, 545-548.
981 Paull, C.K., Neumann, A.C., am Ende, B.A., Ussler, W., Rodriguez, N.M., 2000. Lithoherms on
982 the Florida-Hatteras slope. Marine Geology 166, 83-101.

983 Pedley, H.M., Debono, G., Yeaman, M., 1993. Mesozoic structuring and volcanics along the
984 Pelagian-Ionian boundary: A prelude to foundering of the Ionian Basin, in: Max, M.D.,
985 Colantoni, P. (Eds.), UNESCO Technical Reports in Marine Science, Urbino, pp. 81-86.
986 Piper, D.J.W., Cochonat, P., Morrison, M.L., 1999. The sequence of events around the epicentre
987 of the 1929 Grand Banks earthquake: initiation of debris flows and turbidity currents inferred
988 from sidescan sonar. Sedimentology 46, 79-97.
989 Rebesco, M., Stow, D.A.V., 2001. Seismic expression of contourites and related deposits: A
990 preface. Marine Geophysical Researches 22, 303-308.
991 Reuther, C., 1990. Strike slip generated rifting and recent tectonic stresses on the African
992 foreland (Central Mediterranean region). Annales Tectonicae 4, 120-130.
993 Reuther, C., Ben-Avraham, Z., Grasso, M., 1993. Origin and role of major strike-slip transfers
994 during plate collision in the central Mediterranean. Terra Nova 5, 249-257.
995 Reuther, C.D., Eisbacher, G.H., 1985. Pantelleria rift-crustal extension in a convergent intraplate
996 setting. Geologische Rundschau 74, 585-597.
997 Ryan, W.B.F., Miller, E., 1981. Evidence of a carbonate platform beneath Georges Bank. Marine
998 Geology 44, 213-228.
999 Savini, A., Malinverno, E., Etiope, G., Tessarolo, C., Corselli, C., 2009. Shallow seep-related
1000 seafloor features along the Malta Plateau (Sicily channel – Mediterranean Sea): Morphologies
1001 and geo-environmental control of their distribution. Marine and Petroleum Geology 26, 1831-
1002 1848.
1003 Scandone, P., Patacca, E., Radoicic, R., Ryan, W.B.F., Cita, M.B., Rawson, M., Chezar, H.,
1004 Miller, E., McKenzie, J., Rossi, S., 1981. Mesozoic and Cenozoic rocks from Malta Escarpment
1005 (Central Mediterranean). American Association of Petroleum Geologists Bulletin 65, 1299-1319.

1006 Schlager, W., Reijmer, J.J.G., Droxler, A.W., 1994. Highstand shedding of carbonate platforms.
1007 Journal of Sedimentary Research B64, 270-281.
1008 Seed, H.B., Idriss, A.I., 1971. Simplified procedure for evaluating soil liquefaction potential.
1009 Journal of the Soil Mechanics and Foundations Division 97, 1249-1273.
1010 Siddall, M., Rohling, E.J., Thompson, W.G., Waelbroeck, C., 2008. Marine isotope stage 3 sea
1011 level fluctuations: Data synthesis and new outlook. Reviews of Geophysics 46, RG4003.
1012 Smedile, A., De Martini, P.M., Pantosti, D., Bellucci, L., Del Carlo, P., Gasperini, L., Pirrotta, C.,
1013 Polonia, A., Boschi, E., 2011. Possible tsunami signatures from an integrated study in the
1014 Augusta Bay offshore (Eastern Sicily-Italy). Marine Geology 281, 1-13.
1015 Stow, D.A.V., Faugeres, J.C., Howe, J.A., Pudsey, C.J., Viano, A.R., 2002. Bottom currents,
1016 contourites and deep-sea sediment drifts: Current state-of-the-art, in: Stow, D.A.V., Pudsey, C.J.,
1017 Howe, J.A., Faugeres, J.C., Viano, A.R. (Eds.), Deep-water contourite systems: Modern drifts
1018 and ancient series, seismic and sedimentary characteristics. Geological Society, London, pp. 7-
1019 20.
1020 Strozyk, F., Strasser, M., Forster, A., Kopf, A., Huhn, K., 2010. Slope failure repetition in active
1021 margin environments: Constraints from submarine landslides in the Hellenic fore arc, eastern
1022 Mediterranean. Journal of Geophysical Research 115, B08103.
1023 Tonarelli, B., Turgutcan, F., Max, M.D., Akal, T., 1993. Shallow sediments at four localities on
1024 the Sicilian-Tunisian Platform, in: Max, M.D., Colantoni, P. (Eds.), Geological Development of
1025 the Sicilian-Tunisian Platform. UNESCO, Urbino, pp. 123-128.
1026 Torelli, L., Grasso, M., Mazzoldi, G., Peis, D., Gori, D., 1995. Cretaceous to Neogene structural
1027 evolution of the Lampedusa shelf (Pelagian Sea, Central Mediterranean). Terra Nova 7, 200-212.

1028 Twichell, D.C., Dillon, W.P., Paull, C.K., Kenyon, N.H., 1996. Morphology of carbonate
1029 escarpments as an indicator of erosional processes, in: Gardner, J.V., Field, M.E., Twichell, D.C.
1030 (Eds.), Geology of the United States Seafloor: The View from GLORIA. Cambridge University
1031 Press, Cambridge, pp. 97-108.
1032 Twichell, D.C., Parson, L.M., Paull, C.K., 1990. Variations in the styles of erosion along the
1033 Florida Escarpment, eastern Gulf of Mexico. Marine and Petroleum Geology 7, 253-266.
1034 Volpi, V., Accettella, D., Cuppari, A., 2011. Morphological features of the Apennines
1035 foreland/accretionary-wedge boundary in the Ionian Sea. Marine Geophysical Researches.
1036 Wheeler, A.J., Beyer, A., Freiwald, A., de Haas, H., Huvenne, V.A.I., Kozachenko, M., Olu-Le
1037 Roy, K., Opderbecke, J., 2007. Morphology and environment of cold-water coral carbonate
1038 mounds on the NW European margin. international Journal of Earth Sciences 96, 37-56.
1039 Wiemer, G., Kopf, A., 2015. Altered marine tephra deposits as potential slope failure planes? .
1040 Geo-Marine Letters 35, 305-314.
1041

1042 ## 9. FIGURE LEGENDS

1043

1044 Figure 1: Location map of the north-eastern section of the Pelagian platform and western Ionian
1045 Basin, central Mediterranean Sea. The map displays the principal morphological features, faults
1046 (solid white lines, adapted from Casero et al. (1984) and Gardiner et al. (1995)), and the main
1047 pathways of Modified Atlantic Water (MAW) and Levantine Intermediate Water (LIW) in
1048 eastern Sicily Channel (Béranger et al., 2004; Ciappa, 2009). The background bathymetry is from
1049 EMODnet bathymetry (http://www.emodnet-bathymetry.eu). Inset map is from
1050 www.geomapapp.org.

1051

1052 Figure 2: Multibeam (a) bathymetry and (b) backscatter data from study area. Location of figures
1053 3, 4a-c, 5, and 6 is shown.

1054

1055 Figure 3: Location of gravity cores (pink dots), ROV transects (green dots) and Sparker seismic
1056 reflection profiles (blue lines) acquired from study area. Location of figures 7a,c, 8b, 9a and 11a
1057 is shown.

1058

1059 Figure 4: Seismic stratigraphy of the eastern Malta Plateau. (a) Sparker profile 1 showing a thick
1060 sequence of continuous, parallel, high amplitude seismic reflectors (facies 2A) above an
1061 acoustically transparent seismic facies (facies 3). V.E. stands for vertical exaggeration. (b) Sub-
1062 bottom profile 253 showing a distinct unconformity (unconformity 1) comprising seismic facies
1063 of tilting parallel reflectors (facies 2A) truncated along the western boundary and overlain by a
1064 thin, acoustically transparent facies (facies 1). (c) Sub-bottom profile 030 showing hummocky
1065 topography where acoustically transparent facies (facies 3) is close to the seafloor. Location of
1066 profiles shown in figure 2. (d) Description of the six key seismic facies identified in seismic
1067 reflection profiles across the study area.

1068

1069 Figure 5: (a) Map of principal morphologic elements identified across the southern half of the
1070 study area. (b) Interpretation map of seafloor geomorphic processes across the southern half of
1071 the study area. The continental shelf break is denoted by a dashed black line.

1072

1073 Figure 6: (a) Multibeam bathymetric map of scar S1. (b) Backscatter map of a section of scar S1.

Figure 7: (a) Multibeam bathymetric map of scar S2. (b) Sparker profile 9 intersecting scar S2. Location of profile shown in figure a. The base reflector for scar S2 is the same as for scar S3 (Figure 11d). The failure depth utilised in section 5.2.1.4 is marked. (c) Multibeam backscatter map of scar S2.

Figure 8: (a) Multibeam bathymetric map of scars S3 and S5, showing location of cores CU12_01, 02 and 03. (b) Sparker profile 6 displaying chaotic seismic facies at the location of cores CU12_01 and CU12_03. Location of profile shown in figure a.

Figure 9: (a) Slope gradient map of channel C4. (b) Sparker profile T1 intersecting the upslope section of depression C4. Location of profile shown in figure a. (c) Topographic profile across depression C4. Location of profile shown in figure a. (d) ROV image of steep carbonate outcrops. Location of image is shown in figure a.

Figure 10: Sparker profile 2 intersecting the mound located along the northern flank of depression C4. Location of profile in figure 9a.

Figure 11: (a) Multibeam bathymetry map of elongate ridge along the outer Malta Plateau. Location of figure is shown in figure 3. (b) Sparker profile 3 intersecting the northern section of the ridge. Profile shows a strong reflector that separates an upper unit of sub-parallel, convex upward reflectors (facies 2B) from acoustically transparent facies (facies 3) below. Either side of the ridge, the acoustically transparent facies appears vertically offset. Location of profile is

shown in figure a. (c) Sparker profile 8 intersecting the southern section of the ridge. Profile shows the ridge to be characterised by acoustically transparent facies (facies 3) that is vertically offset along the western flank. Upslope of the ridge, the shallow stratigraphy comprises parallel to sub-parallel reflections (facies 2A) that can be sub-divided into two sub-facies. The deeper of these (facies 2A-2) is offset in the eastern part. Location of profile is shown in figure a. (d) Sparker profile 6 intersecting scar S3 and the central section of the ridge. Location of profile is shown in figure a. (e) ROV image of carbonate hardground. Location of image is shown in figure a. (f) Dredged sample of carbonate hardground from ROV transect. Location of sample is shown in figure a.

Figure 12: Gravity core correlation panels from (a) the northern part of the study area, at channel C4, (b) the central area, at scar S2, and (c) the southern area, at scar S5. (d) Correlation panel across the three areas based on the three cores that were taken from undisturbed seafloor, i.e. outside the influence of scar or channel. The soldi lines represent confident correlations and the dashed lines possible correlations. Note (i) the amount of time "locked" in facies C1 in core CU12_07 in panel (a), (ii) the lack of slide deposits in the cores from scar S2 in panel (b), (iii) the relative stratigraphic positions of facies D and the facies E in panel (c), and (iv) the sharp increase in density (and changes in the other properties) in core CU12_02 below the thin sandy layer, which we interpret as a turbidite-draped erosional surface. For core locations see figure 3.

Figure 13: (a) Scanning electron microscope image of the ash from core CU12_01. (b) Total Alkali Silica classification diagram (Le Bas et al., 1986) showing glass compositions of the studied samples (in red) and glass compositions of the 122 BC tephra recovered in MS6 core in

1120 Augusta Bay, Ionian Sea (Smedile et al., 2011), Priolo Reserve site (OPR-S6 and OPR-S10
1121 cores; (De Martini et al., 2010)) and from Etna flanks (122 BC glass) for comparison. Dashed
1122 line includes the composition of Etna volcanics (Corsaro and Pompilio, 2004).
1123
1124 Figure 14: (a-d) Plots of undrained shear strength (Cu) data from vane shear testing against depth
1125 down core (below seafloor) for cores CU12_01, 02, 07 and 10. (e) Plot for data from all these
1126 cores (excluding anomalously high values of undrained shear strength (>10 kPa) from core
1127 CU12_02) clearly indicates an increase of shear strength with depth and an average strength
1128 increase rate of 2.37 kPa/m.
1129
1130 Figure 15: (a) Regression curve for analysis of pseudostatic slope stability indicating required
1131 seismic coefficient to reduce the factor of safety for the slope to 1.0. (b) Seismic hazard curve for
1132 the landslide site from model available at
1133 http://www.efehr.org:8080/jetspeed/portal/HazardMaps.psml.
1134

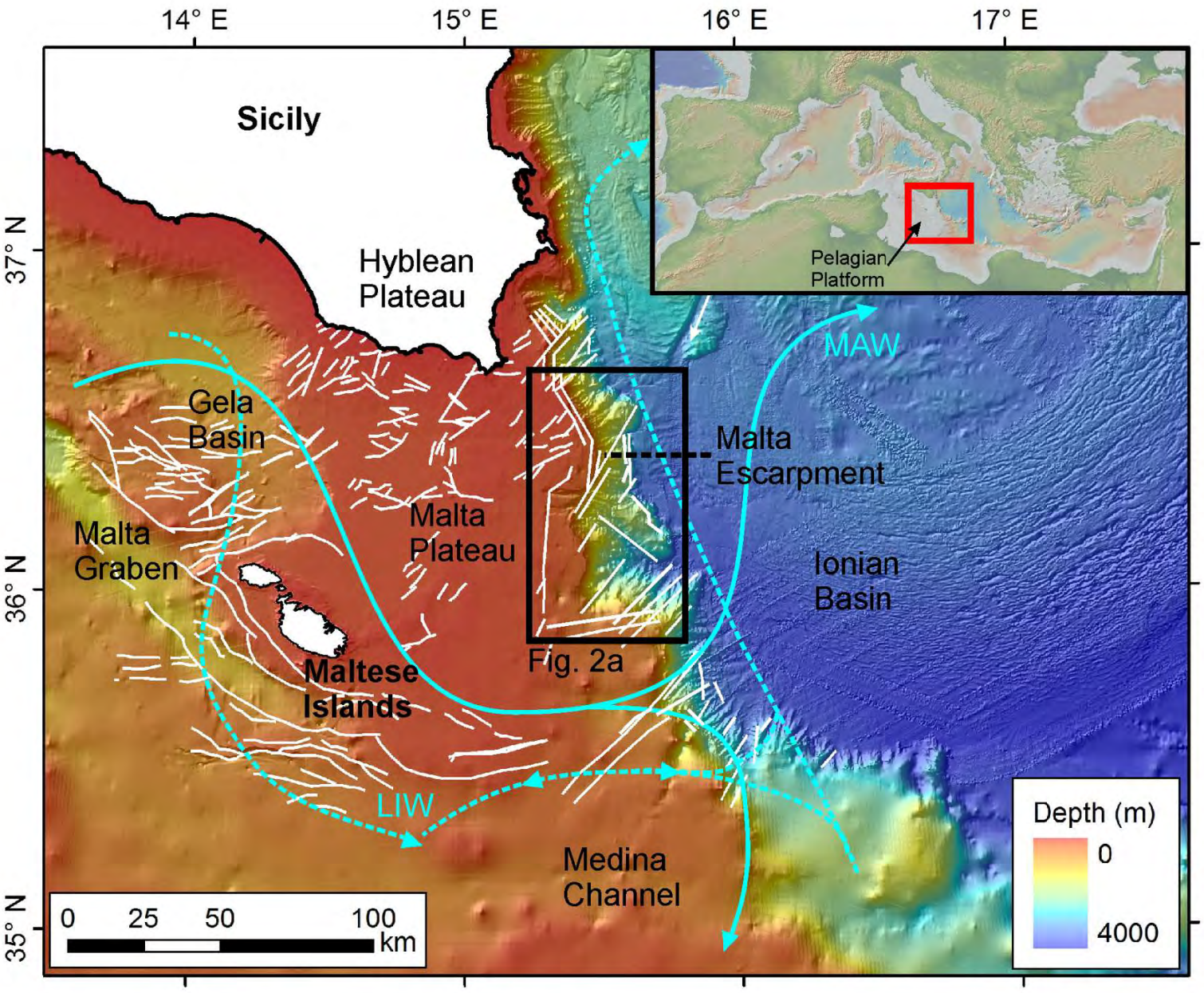
14° E
15° E
16° E
17° E
37° N
36° N
35° N
Sicily
Hyblean
Plateau
Pelagian
Platform
MAW
Gela
Basin
Malta
Escarpment
Malta
Plateau
Malta
Graben
Ionian
Basin
Fig. 2a
Maltese
Islands
LIW
Medina
Channel
Depth (m)
0
4000
0
25
50
100
km

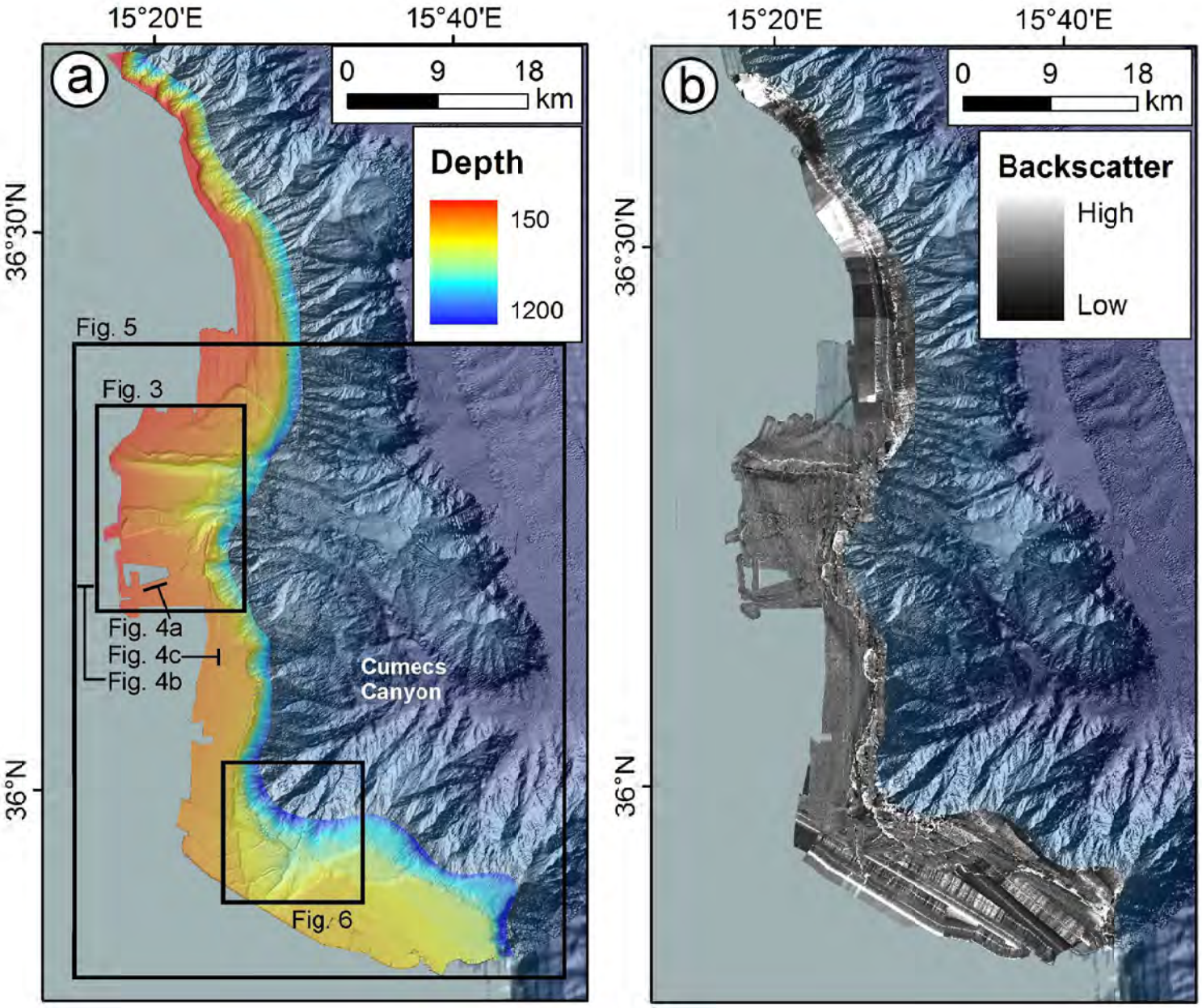
a
b
15°20'E
15°40'E
36°30'N
36°N
0
9
18
km
Depth
150
1200
Backscatter
High
Low
Fig. 5
Fig. 3
Fig. 4a
Fig. 4c
Fig. 4b
Fig. 6
Cumecs
Canyon

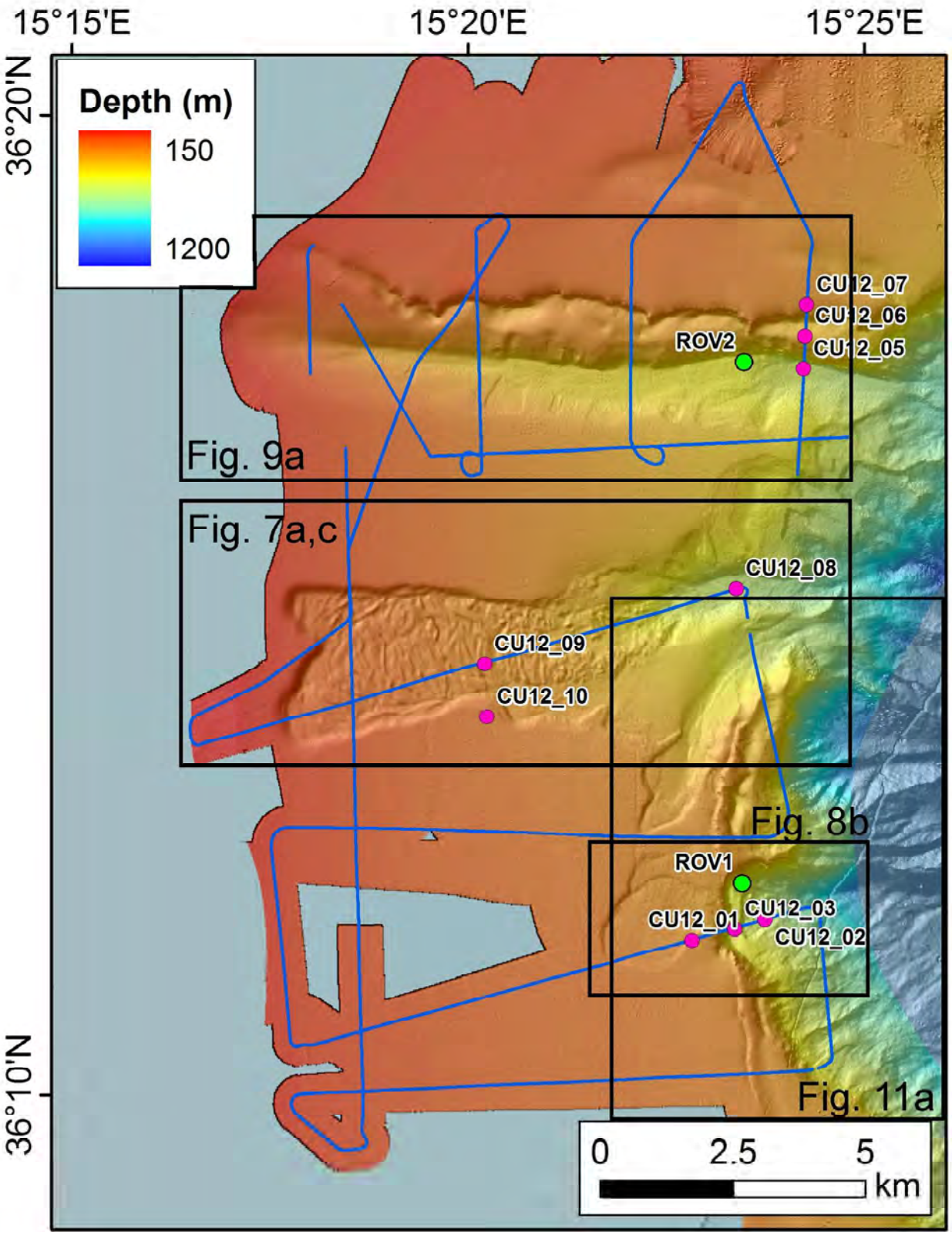
15°15'E
15°20'E
15°25'E
36°20'N
36°10'N
Depth (m)
150
1200
CU12_07
CU12_06
CU12_05
ROV2
Fig. 9a
Fig. 7a,c
CU12_08
CU12_09
CU12_10
Fig. 8b
ROV1
CU12_01
CU12_03
CU12_02
Fig. 11a
0
2.5
5
km

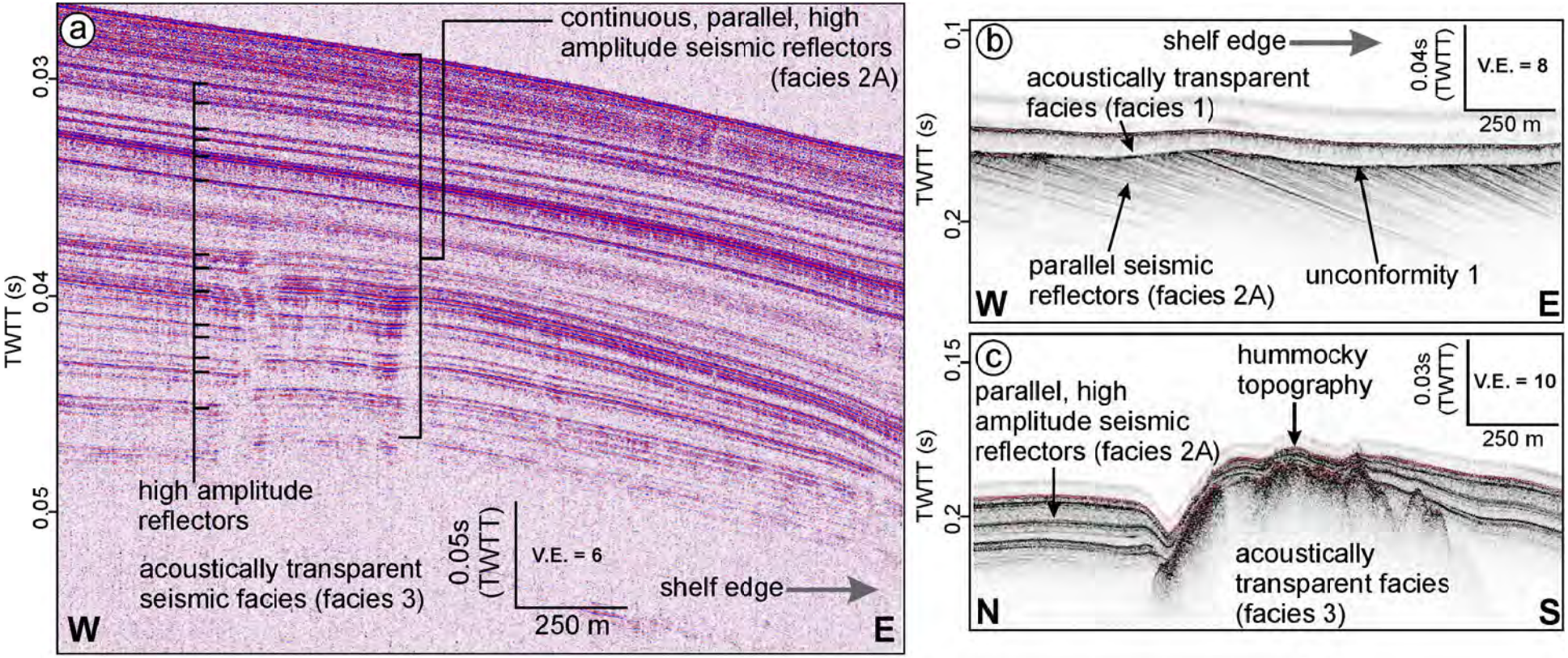

d

Facies	Description
1	acoustically transparent seismic facies with continuous, regular, high amplitude reflector at the top
2A	sequence of continuous, parallel, high amplitude seismic reflectors
2B	sequence of sub-parallel, upwardly-convex, high-amplitude seismic reflectors
2C	sequence of chaotic seismic facies
2D	acoustically transparent seismic facies with discontinuous, irregular, variable amplitude reflector at the top
3	acoustically transparent seismic facies with discontinuous, irregular, variable amplitude reflector at the top

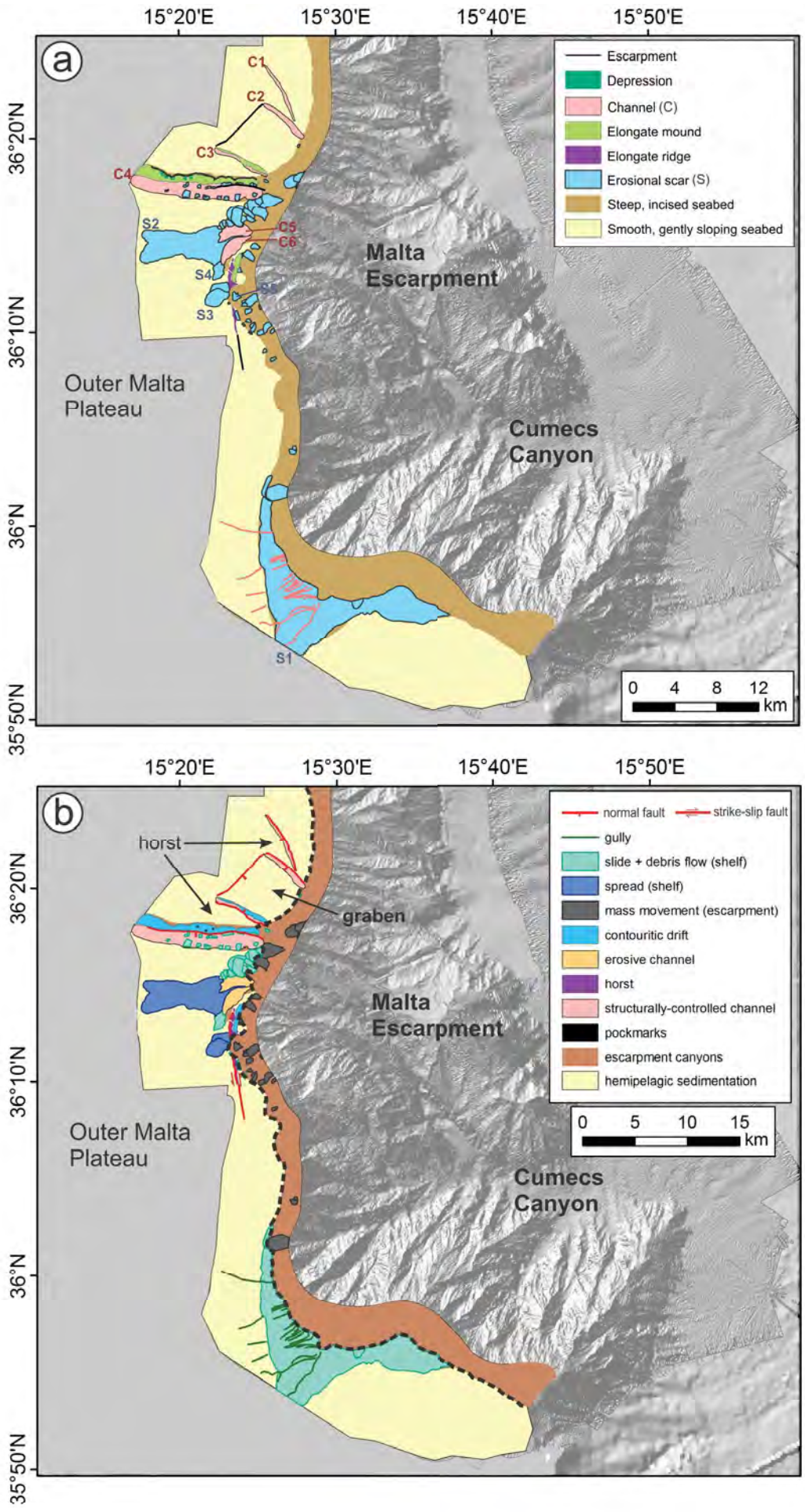
a
15°20'E
15°30'E
15°40'E
15°50'E
36°20'N
36°10'N
36°N
35°50'N
C1
C2
C3
C4
C5
C6
S1
S2
S3
S4
Malta Escarpment
Outer Malta Plateau
Cumecs Canyon
Escarpment
Depression
Channel (C)
Elongate mound
Elongate ridge
Erosional scar (S)
Steep, incised seabed
Smooth, gently sloping seabed
0 4 8 12
km
b
15°20'E
15°30'E
15°40'E
15°50'E
36°20'N
36°10'N
36°N
35°50'N
horst
graben
Malta Escarpment
Outer Malta Plateau
Cumecs Canyon
normal fault
strike-slip fault
gully
slide + debris flow (shelf)
spread (shelf)
mass movement (escarpment)
contouritic drift
erosive channel
horst
structurally-controlled channel
pockmarks
escarpment canyons
hemipelagic sedimentation
0 5 10 15
km

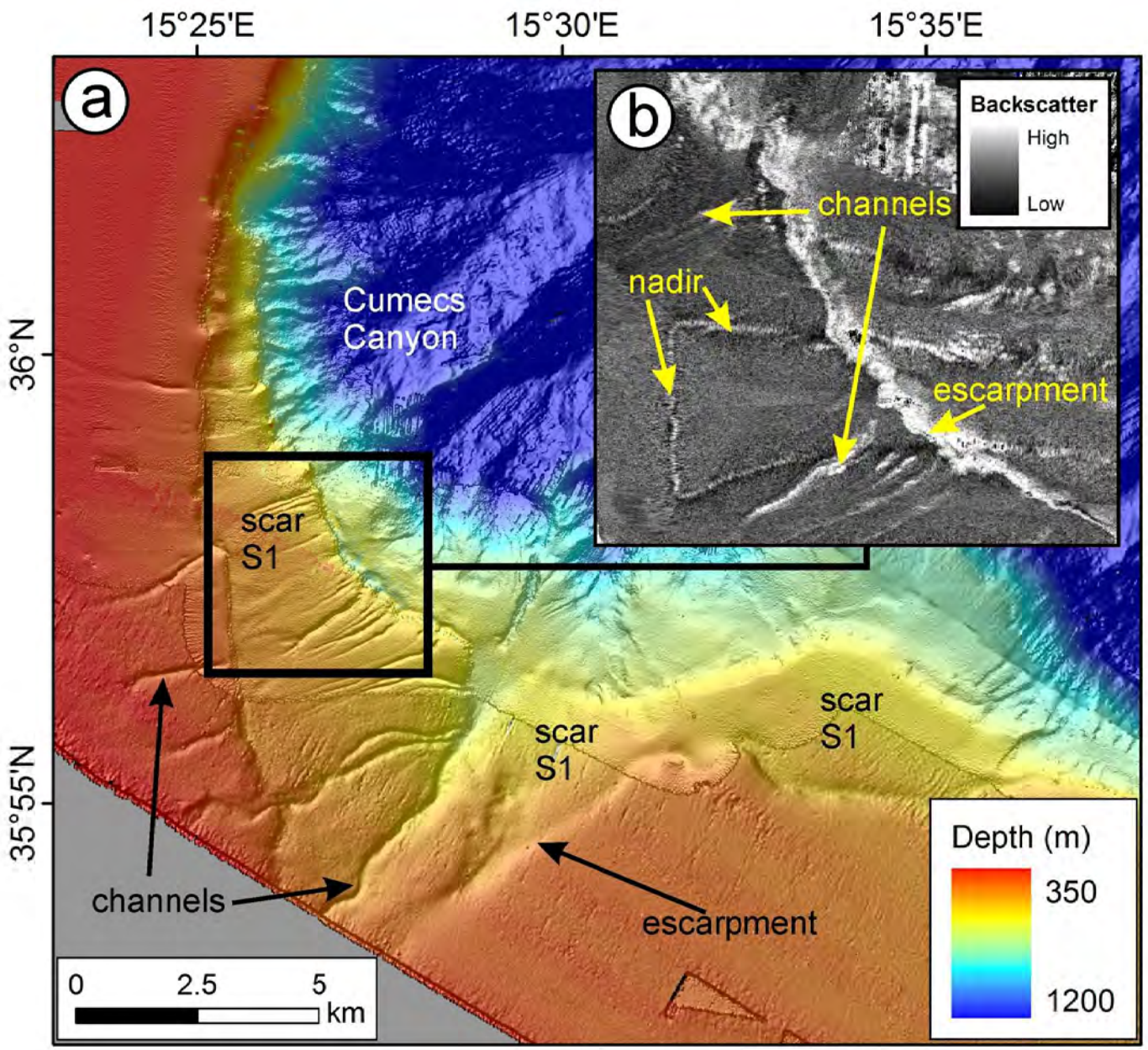
15°25'E
15°30'E
15°35'E
36°N
35°55'N
a
b
Backscatter
High
Low
channels
nadir
escarpment
Cumecs
Canyon
scar
S1
scar
S1
scar
S1
channels
escarpment
Depth (m)
350
1200
0
2.5
5
km

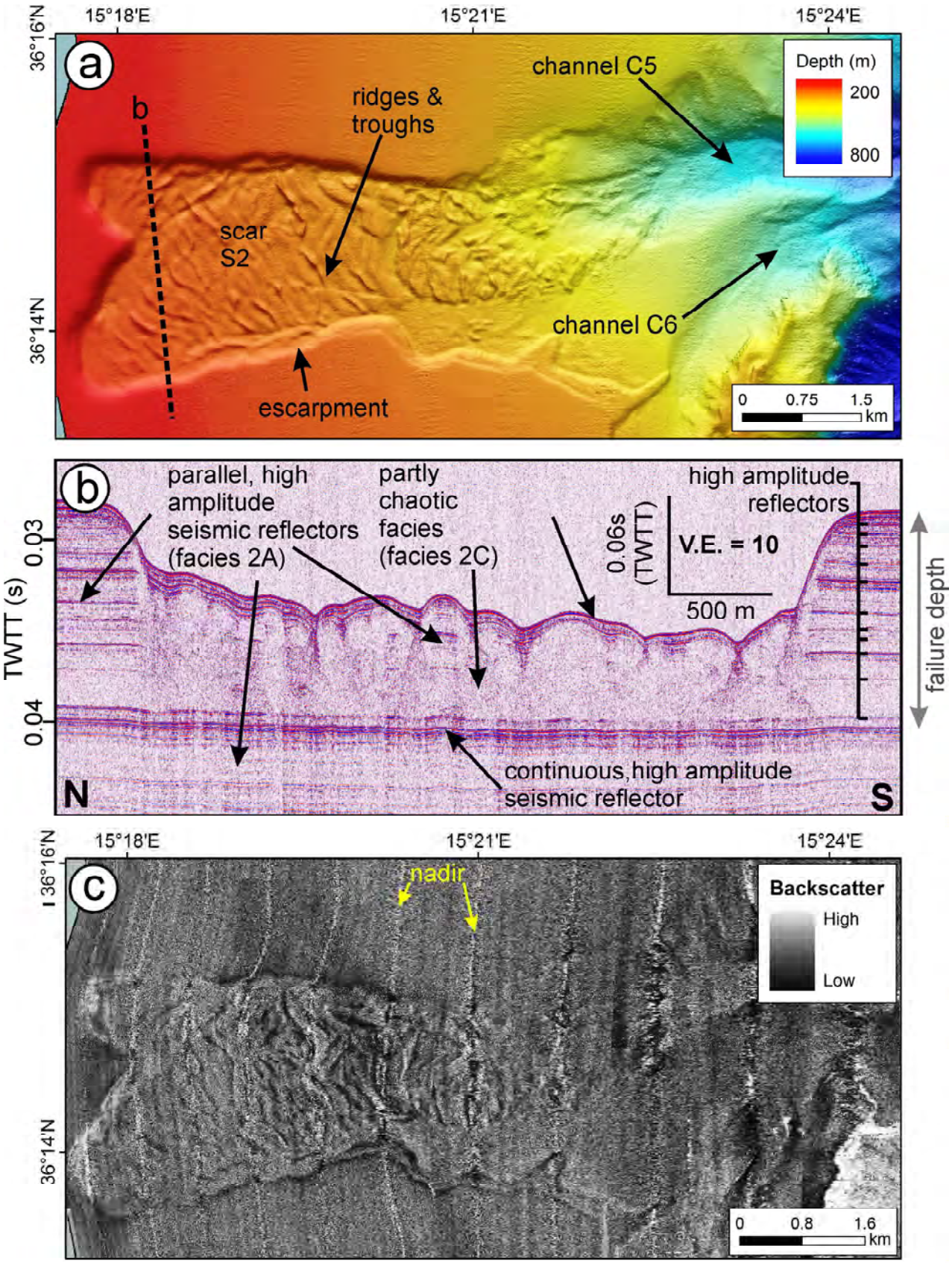
a
15°18'E
15°21'E
15°24'E
36°16'N
36°14'N
b
ridges &
troughs
channel C5
Depth (m)
200
800
scar
S2
channel C6
escarpment
0
0.75
1.5
km
b
parallel, high
amplitude
seismic reflectors
(facies 2A)
partly
chaotic
facies
(facies 2C)
high amplitude
reflectors
0.06s
(TWTT)
V.E. = 10
500 m
TWTT (s)
0.03
0.04
failure depth
continuous, high amplitude
seismic reflector
N
S
c
15°18'E
15°21'E
15°24'E
36°16'N
36°14'N
nadir
Backscatter
High
Low
0
0.8
1.6
km

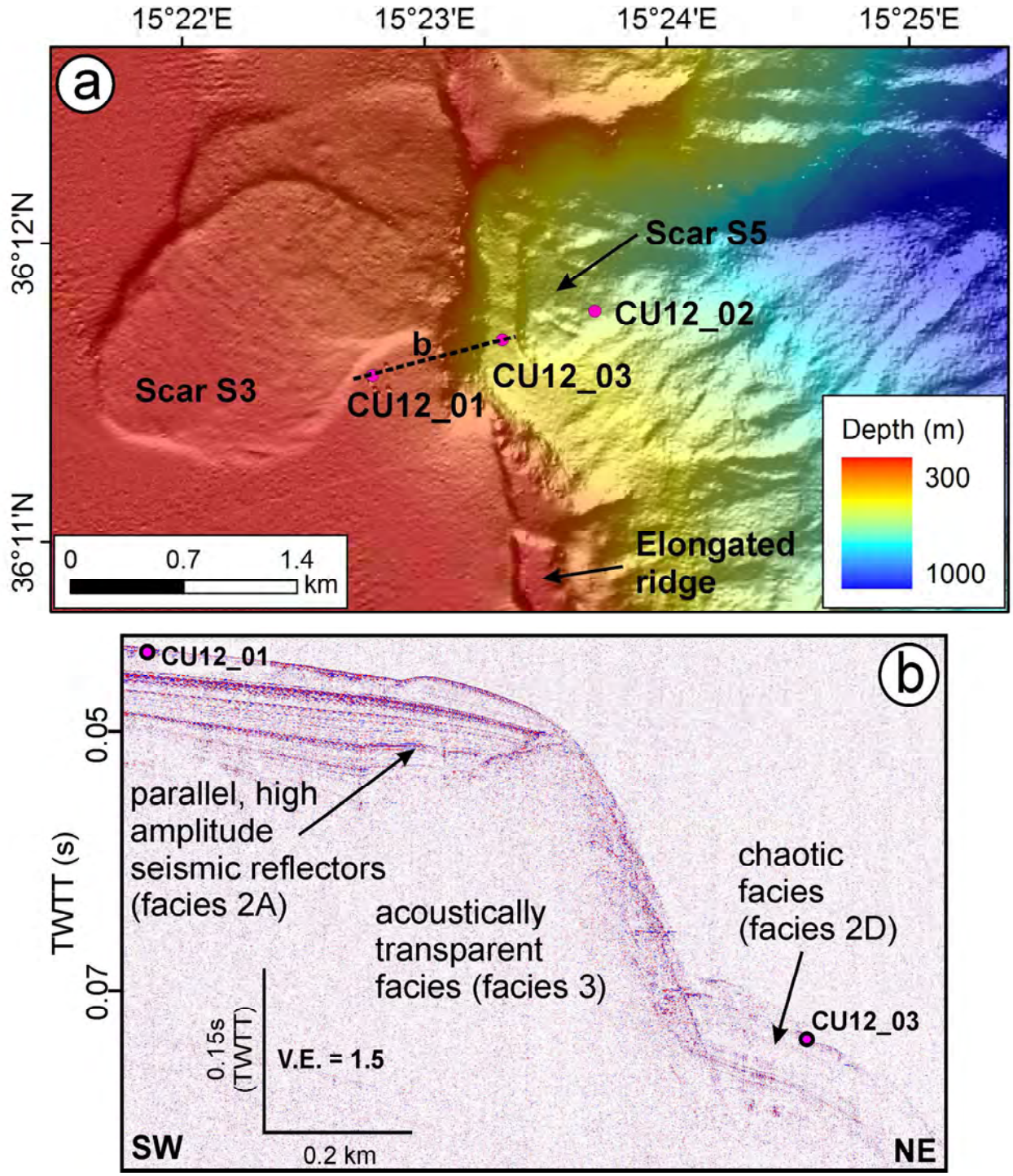
15°22'E
15°23'E
15°24'E
15°25'E
36°12'N
36°11'N
a
Scar S5
CU12_02
b
CU12_03
CU12_01
Scar S3
Depth (m)
300
1000
0
0.7
1.4
km
Elongated
ridge
b
CU12_01
0.05
0.07
TWTT (s)
parallel, high
amplitude
seismic reflectors
(facies 2A)
acoustically
transparent
facies (facies 3)
chaotic
facies
(facies 2D)
CU12_03
0.15s
(TWTT)
V.E. = 1.5
0.2 km
SW
NE

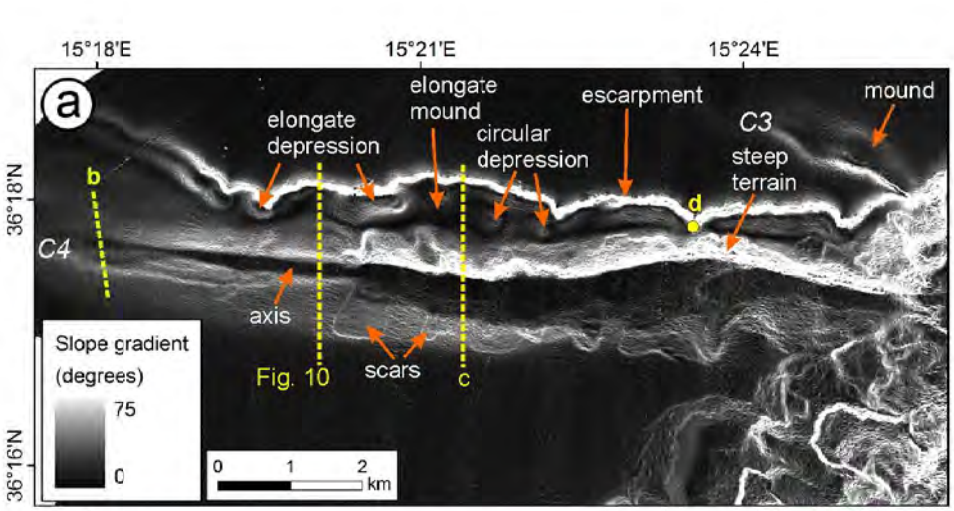
a
15°18'E
15°21'E
15°24'E
36°18'N
36°16'N
elongate depression
elongate mound
circular depression
escarpment
mound
C3
steep terrain
C4
b
c
d
axis
scars
Fig. 10
Slope gradient (degrees)
75
0
0 1 2 km

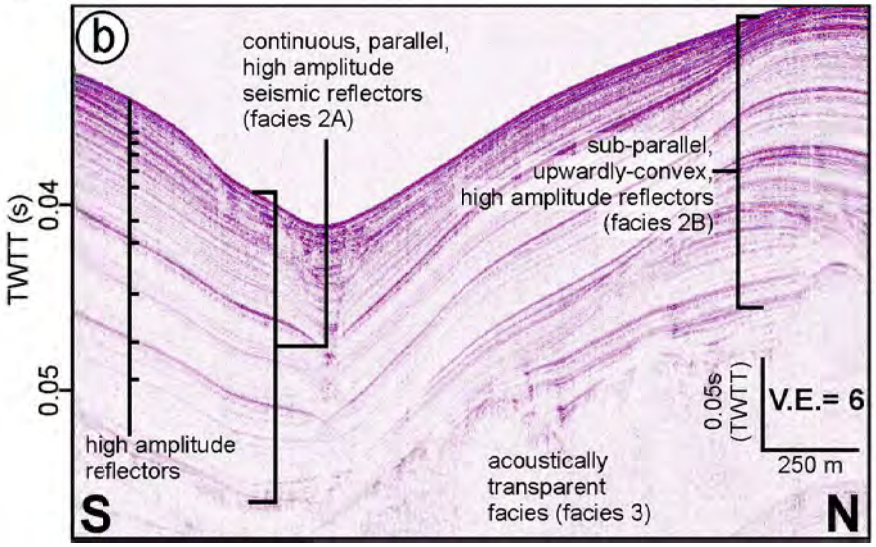
b
continuous, parallel, high amplitude seismic reflectors (facies 2A)
sub-parallel, upwardly-convex, high amplitude reflectors (facies 2B)
TWTT (s)
0.04
0.05
high amplitude reflectors
acoustically transparent facies (facies 3)
0.05s (TWTT)
V.E.= 6
250 m
S
N

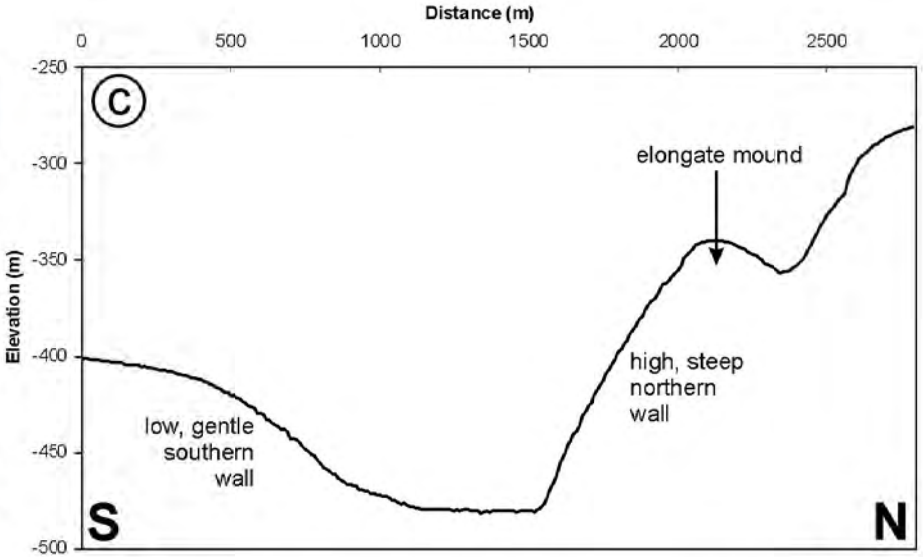
c
Distance (m)
0
500
1000
1500
2000
2500
Elevation (m)
-250
-300
-350
-400
-450
-500
elongate mound
high, steep northern wall
low, gentle southern wall
S
N


d
0.4 m
CUMECS12
*H 8 D 343 12:44:52 01/07/12

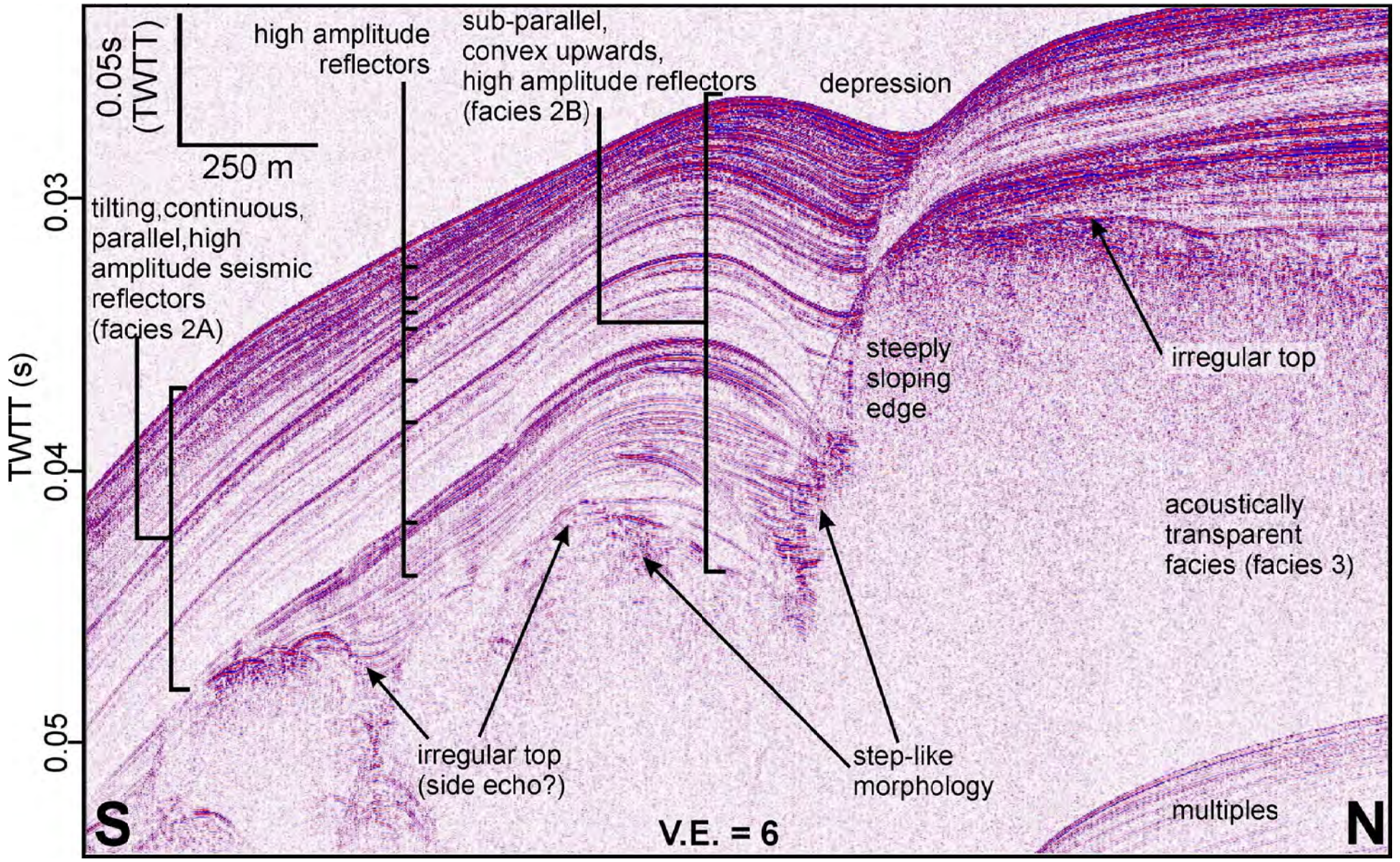
0.05s (TWTT)
250 m
high amplitude reflectors
sub-parallel, convex upwards, high amplitude reflectors (facies 2B)
depression
tilting,continuous, parallel,high amplitude seismic reflectors (facies 2A)
steeply sloping edge
irregular top
acoustically transparent facies (facies 3)
irregular top (side echo?)
step-like morphology
multiples
S
N
V.E. = 6
TWTT (s)
0.03
0.04
0.05

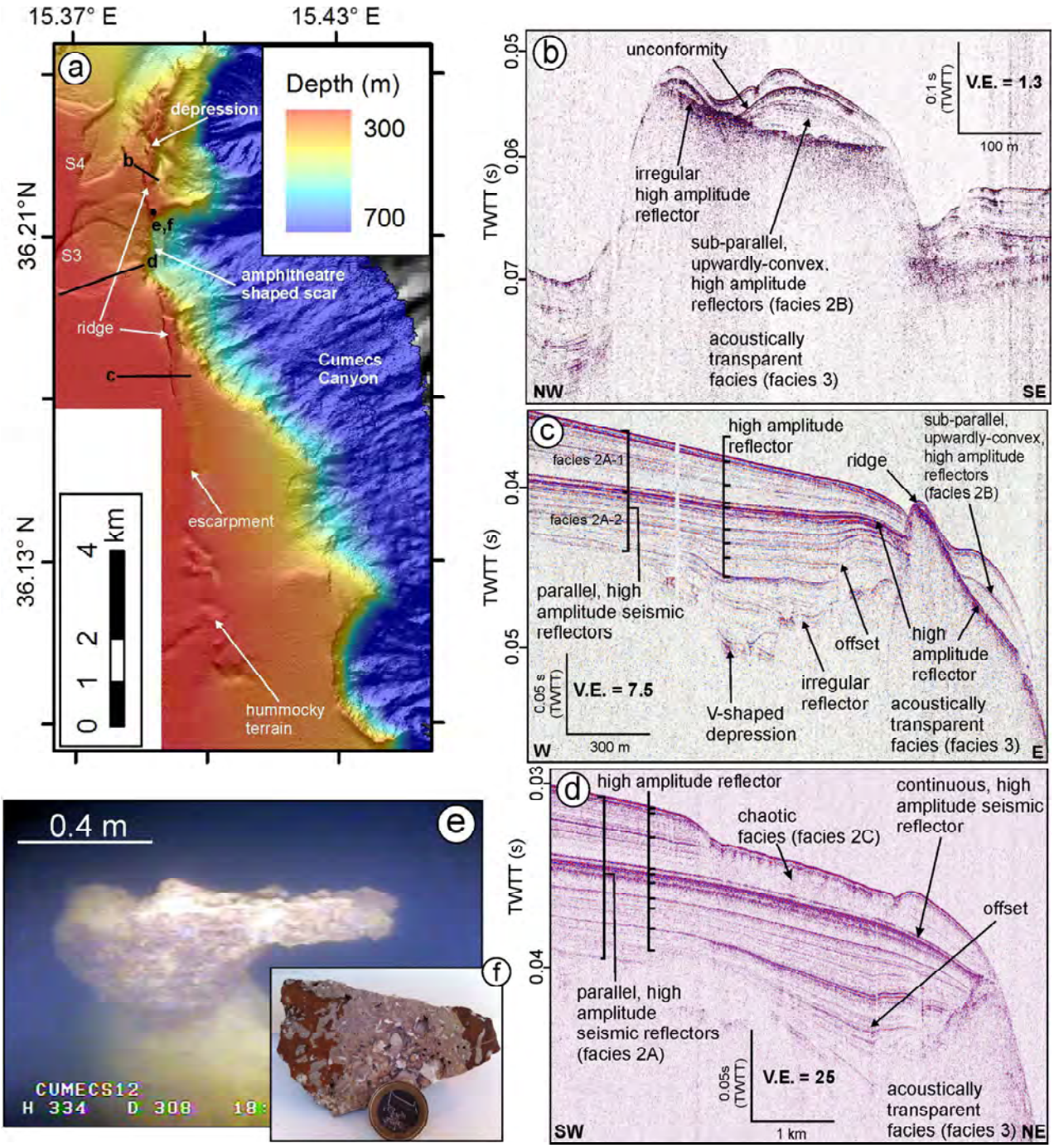
15.37° E
15.43° E
36.21°N
36.13° N
a
Depth (m)
300
700
depression
S4
b
e,f
S3
d
amphitheatre shaped scar
ridge
c
Cumecs Canyon
escarpment
hummocky terrain
0 1 2 4 km
b
unconformity
0.1 s (TWTT)
V.E. = 1.3
100 m
irregular high amplitude reflector
sub-parallel, upwardly-convex, high amplitude reflectors (facies 2B)
acoustically transparent facies (facies 3)
NW
SE
TWTT (s)
0.05
0.06
0.07
c
facies 2A-1
facies 2A-2
high amplitude reflector
ridge
sub-parallel, upwardly-convex, high amplitude reflectors (facies 2B)
parallel, high amplitude seismic reflectors
offset
high amplitude reflector
irregular reflector
V-shaped depression
acoustically transparent facies (facies 3)
0.05 s (TWTT)
V.E. = 7.5
300 m
W
E
0.04
0.05
e
0.4 m
CUMECS12
H 334 D 308
f
d
high amplitude reflector
chaotic facies (facies 2C)
continuous, high amplitude seismic reflector
offset
parallel, high amplitude seismic reflectors (facies 2A)
0.05s (TWTT)
V.E. = 25
1 km
acoustically transparent facies (facies 3)
SW
NE
0.03
0.04

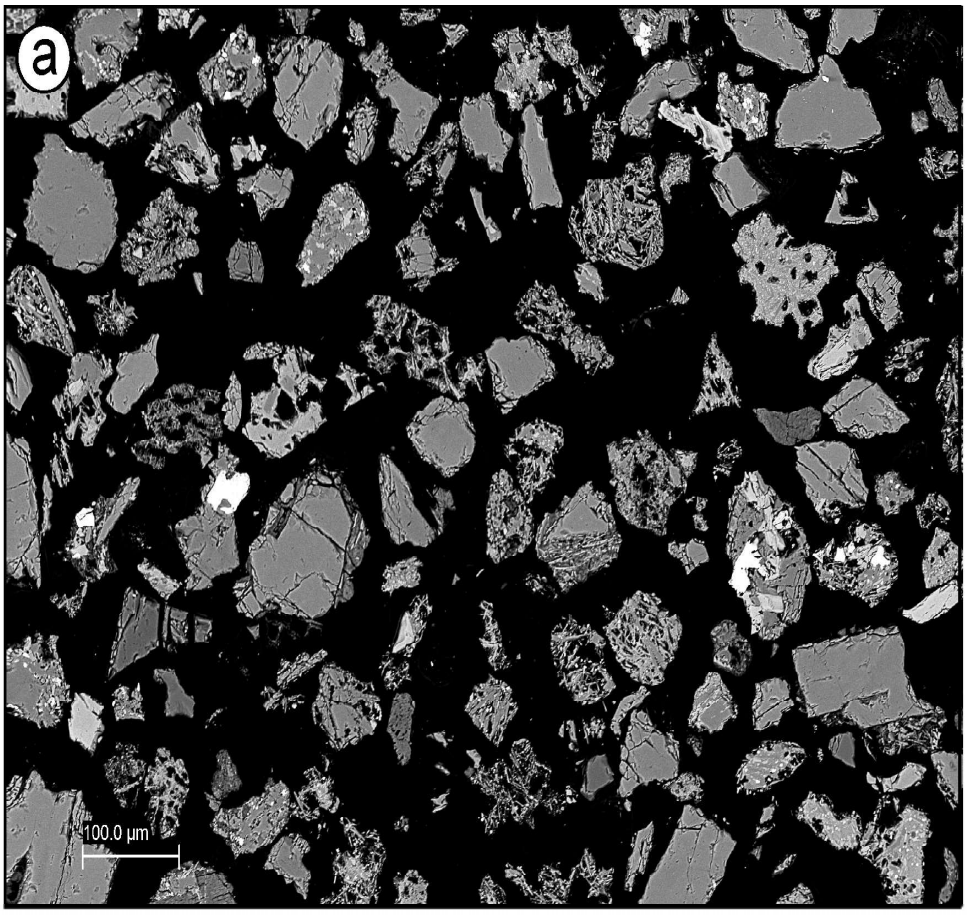
a
100.0 µm

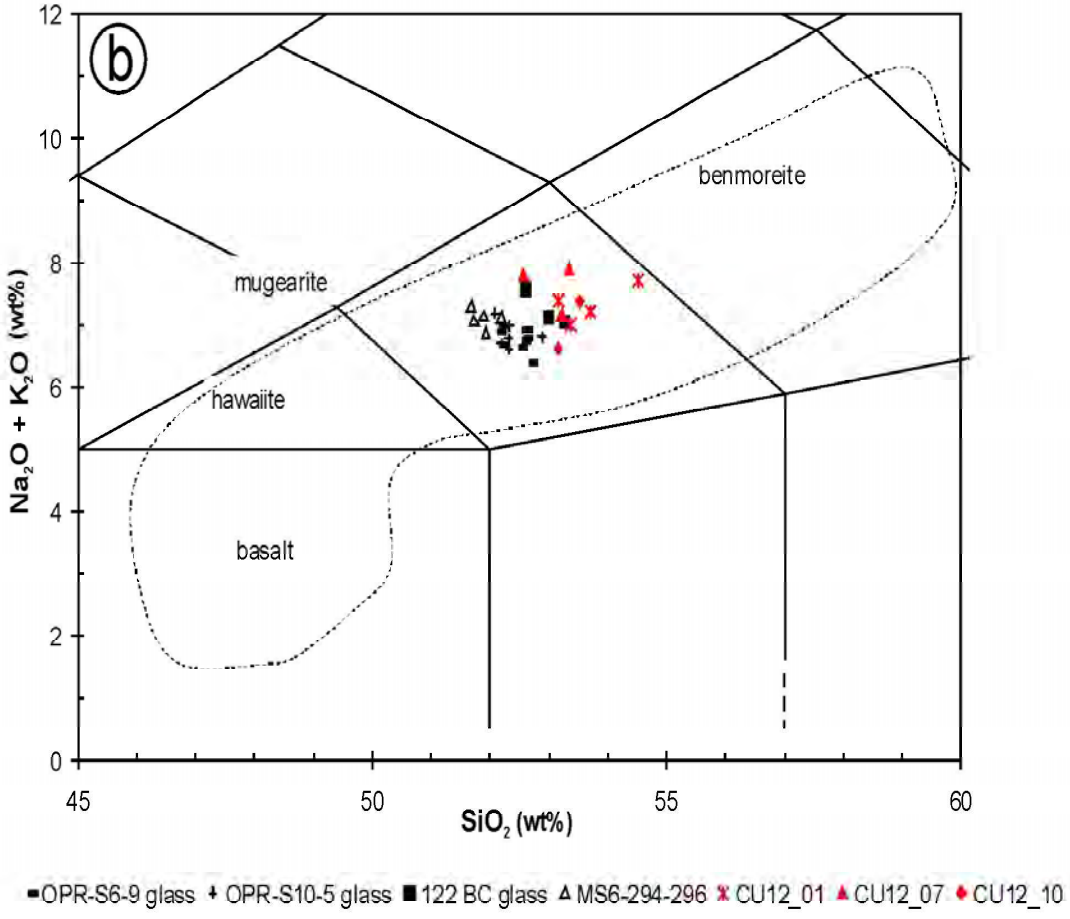
b
benmoreite
mugearite
hawaiite
basalt
Na2O + K2O (wt%)
SiO2 (wt%)
0
2
4
6
8
10
12
45
50
55
60
OPR-S6-9 glass
OPR-S10-5 glass
122 BC glass
MS6-294-296
CU12_01
CU12_07
CU12_10

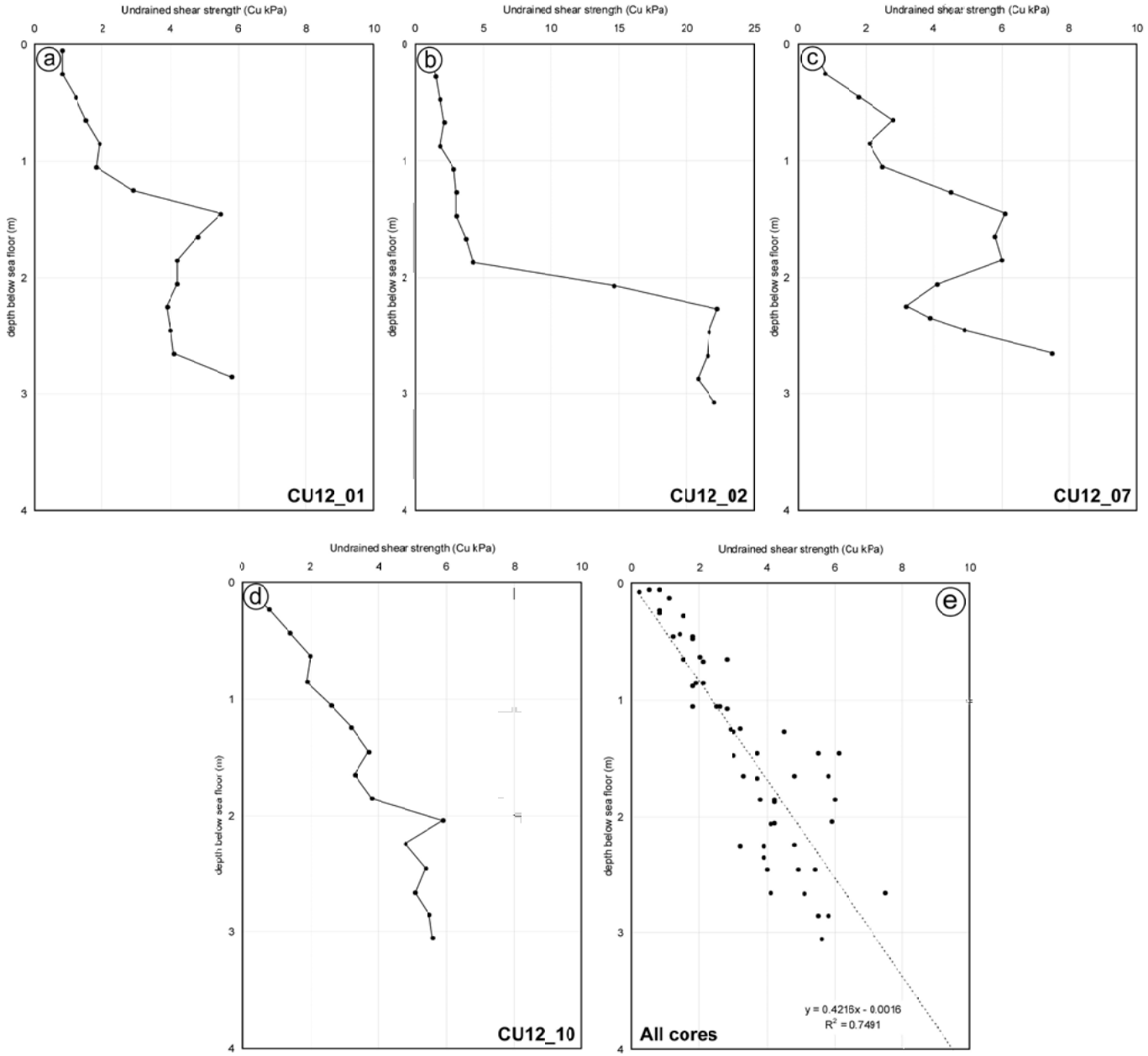
Undrained shear strength (Cu kPa)
depth below sea floor (m)
a
CU12_01
b
CU12_02
c
CU12_07
d
CU12_10
e
All cores
y = 0.4215x - 0.0016
R² = 0.7491

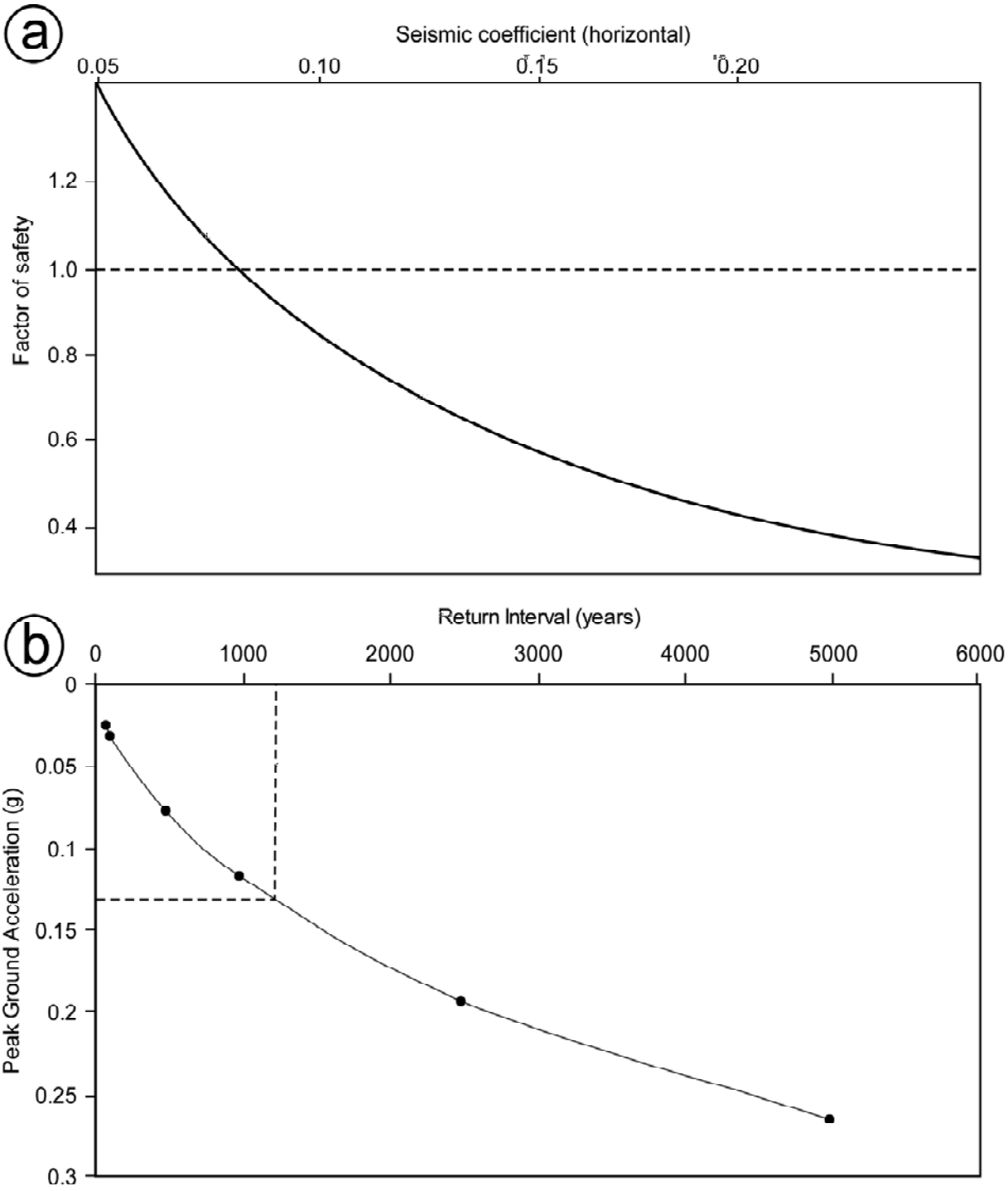
a
Seismic coefficient (horizontal)
0.05
0.10
0.15
0.20
Factor of safety
1.2
1.0
0.8
0.6
0.4
b
Return Interval (years)
0
1000
2000
3000
4000
5000
6000
Peak Ground Acceleration (g)
0
0.05
0.1
0.15
0.2
0.25
0.3

Highlights

- We investigate geomorphic processes in the outer shelf of a carbonate escarpment
- Study is based on geophysical, sedimentological and visual data from Malta Plateau
- Erosional scars, channels, elongate mounds, and an elongate ridge are documented
- Key processes are slope instability, strike-slip deformation, bottom current flow
- Outer shelf geomorphology is directly influenced by escarpment-forming processes